DISEASES AND DISORDERS

Targeting the NEDP1 enzyme to ameliorate ALS phenotypes through stress granule disassembly

Toufic Kassouf[1]†‡, Rohit Shrivastava[1]†, Igor Meszka[1], Aymeric Bailly[1], Jolanta Polanowska[1], Helene Trauchessec[1], Jessica Mandrioli[2,3], Serena Carra[3], Dimitris P. Xirodimas[1]*

The elimination of aberrant inclusions is regarded as a therapeutic approach in neurodegeneration. In amyotrophic lateral sclerosis (ALS), mutations in proteins found within cytoplasmic condensates called stress granules (SGs) are linked to the formation of pathological SGs, aberrant protein inclusions, and neuronal toxicity. We found that inhibition of NEDP1, the enzyme that processes/deconjugates the ubiquitin-like molecule NEDD8, promotes the disassembly of physiological and pathological SGs. Reduction in poly(ADP-ribose) polymerase1 activity through hyper-NEDDylation is a key mechanism for the observed phenotype. These effects are related to improved cell survival in human cells, and in *C. elegans*, *nedp1* deletion ameliorates ALS phenotypes related to animal motility. Our studies reveal NEDP1 as potential therapeutic target for ALS, correlated to the disassembly of pathological SGs.

INTRODUCTION

Organisms are constantly exposed to environmental stresses that cause protein damage and the generation of RNA-protein inclusions. A series of sophisticated mechanisms that constitute the so-called protein quality control (PQC) system ensure the detection, repair, and/or elimination of damaged proteins and dissolution of inclusions to maintain protein homeostasis (*1*). Two main types of proteinaceous assemblies can be induced upon stress: aggregates or inclusions that are mainly composed of terminally misfolded proteins and biomolecular condensates that often contain proteins and nucleic acids (*1*–*3*). Although both depend on the PQC system for dispersal, proteinaceous aggregates and condensates show different properties. Aggregates are static structures that require disaggregation or digestion mechanisms for their removal (*3*). Instead, stress-induced condensates are more dynamic and form through principles of liquid-liquid phase separation (LLPS) (*2*, *4*, *5*). However, condensates can convert into more solid-like fibrillar states, also ultimately generating aggregates (*4*–*8*).

One typical example of stress-induced condensates is represented by stress granules (SGs), RNA-protein assemblies that are rapidly formed in the cytoplasm upon stress conditions, including heat shock, oxidative stress, viral infection, and proteasome inhibition. The generation of SGs is part of the response to modulate several cellular activities, including reduction of protein synthesis of housekeeping mRNAs during stress, and to protect selected mRNAs from degradation (*9*–*11*). Their formation is initiated by the assembly of core proteins around stalled mRNAs, followed by their nucleation mainly with RNA binding proteins that form the shell. Upon stress alleviation, SGs are disassembled, allowing protein synthesis resumption and cell recovery (*9*–*11*).

However, defects at the level of SG assembly/disassembly can cause the aberrant conversion of SGs from liquid-like dynamic condensates into aggregated-like structures, referred to as aberrant or pathological SGs. The presence of aberrant SGs that persist in the cytoplasm has been associated to several neurodegenerative diseases, such as amyotrophic lateral sclerosis (ALS) or frontotemporal dementia (FTD) (*12*, *13*). Different mechanisms have been proposed for these defects in SG dynamics. First, mutations in genes that encode for SG proteins (e.g., TDP-43, FUS, and TIA1) usually occur in the intrinsically disordered regions, which are key regulatory modules of LLPS and SG dynamics. These mutations confer higher aggregation propensities to these proteins and promote the maturation of liquid-like SGs into aberrant SGs that can further evolve with time into proteinaceous inclusions that persist in the cytoplasm (*14*–*18*). Second, failure of the PQC system to clear mutated and misfolded SG proteins, or defective ribosomal products that can accumulate within SGs, promotes their conversion into a solid-like aberrant state (*16*, *19*, *20*). As a result, SGs fail to disassemble upon stress relief, leading to protein synthesis deficiency and contributing to neuronal cell death (*17*). However, the direct link between aberrant SG formation and ALS pathology is still unclear, as exemplified by the study of ALS-derived mutants of TDP-43 protein that can induce cytoplasmic aggregates and ALS-related pathology, independently of SGs (*21*–*23*). Nevertheless, it is evident that, independently on whether they mainly derive from either direct deposition or maturation of SGs into an aggregated-like state, proteinaceous inclusions enriched for mutant TDP-43 or FUS are associated with cell toxicity (*17*, *22*–*24*). Thus, acceleration of the elimination of toxic protein inclusions is regarded as an attractive approach to potentially reestablish normal neuronal function. Toward this goal, several strategies have been proposed, including the use of antisense oligonucleotides that reduce the levels of mutant aggregation-prone proteins, antibodies that target aggregates containing mutated SG proteins, boosting the proteasome and/or autophagy pathways, which are the main elements of the PQC system that clear misfolded proteins and aberrant inclusions (*24*–*28*).

[1]CRBM, Univ. Montpellier, CNRS, Montpellier, France. [2]Neurology Unit, Azienda Ospedaliero Universitaria di Modena, 41126 Modena, Italy. [3]Department of Biomedical, Metabolic and Neural Sciences, University of Modena and Reggio Emilia,G. Campi 287, 41125 Modena, Italy.
†These authors contributed equally to this work.
‡Present address: Dioscuri Centre for Metabolic Diseases, Nencki Institute of Experimental Biology, Polish Academy of Sciences, 3 Pasteur Street, 02-093 Warsaw, Poland.
*Corresponding author. Email: dimitris.xirodimas@crbm.cnrs.fr

Among the main effectors and regulators of the PQC system is the family of ubiquitin and ubiquitin-like molecules (Ubls) such as SUMO and NEDD8. Their covalent modification on substrate proteins, referred to as ubiquitination, SUMOylation, and NEDDylation, occurs via a three-step process involving E1, E2, and E3 enzymes and are regarded as key regulators of protein oligomerization and assembly into macromolecular complexes (*1*, *29*–*31*). Since they all target mainly lysine residues, competition and cooperation between ubiquitination, SUMOylation, and NEDDylation occurs, tightly regulating the substrate activity or fate (*32*). Several lines of evidence have indicated that ubiquitination and SUMOylation control the SG proteome composition and the dynamics of SG assembly and disassembly, even if their role may be dependent on cell type and applied stress (*33*–*39*). These findings further underscore the existence of a tight interplay between the PQC system and SG dynamics. In a small interfering RNA screen for factors that control SG dynamics, components of the NEDD8 pathway were identified (*40*). The studies suggested that NEDDylation of the serine/arginine (SR)–rich family member protein SRSF3, which is found within SGs upon oxidative stress (sodium arsenite), is required for SG assembly. The role of NEDD8 remains somehow elusive (*32*), as later studies using short-term chemical inhibition of the NEDD8 and ubiquitin E1 activating enzymes indicated that the NEDD8 and ubiquitin pathways are not implicated in the control of SG dynamics upon arsenite-induced stress (*41*).

Protein modification with ubiquitin/Ubls is a reversible process, and the extent of substrate modification is finely balanced by the coordinated action of conjugating and deconjugating enzymes (*31*, *42*). For the NEDD8 pathway, there are two highly specific deconjugating enzymes, the COP9 signalosome and NEDP1 (*29*, *43*). NEDP1 also processes NEDD8 into the mature form, before activation by the NEDD8 E1 activating enzyme (NAE) (*32*). COP9 is a well-established regulator of the activity of the cullin-ring ligases through deNEDDylation of cullins; by contrast, our knowledge on processes controlled by NEDP1 is limited (*32*, *44*). On the basis of the highly specific activity of NEDP1 to deconjugate NEDD8, understanding the biological role of this enzyme will also help elucidating processes controlled by protein NEDDylation (*32*, *45*–*47*).

Here, we identify NEDP1 as critical regulator of SG dynamics. NEDP1 knockout (KO), as well as inhibition of NEDP1 by expression of anti-NEDP1 nanobody (Nb), promotes the disassembly of SGs. Proteome-wide analysis of NEDDylation sites at endogenous levels of wild-type NEDD8 expression combined with mutational analysis identified the poly(ADP-ribose) polymerase 1 (PARP-1) as NEDP1 substrate. PARP-1 hyper-NEDDylation reduces the generation of PAR conjugates, which are important regulators of SG dynamics (*21*, *48*, *49*). Critically, we found that NEDP1 inhibition in several in vitro systems, including ALS patient–derived fibroblasts, also promotes the disassembly of aberrant SGs. Using two *Caenorhabditis elegans* ALS models (*sod-1*^{G85R}, *C9orf72* G4C2 expansion), we found that *nedp1* (*ulp-3*) deletion ameliorates ALS phenotypes related to animal motility. Our studies identify NEDP1 as a critical regulator of SG dynamics and a potential therapeutic target for ALS.

RESULTS

NEDP1 inhibition accelerates the formation and disassembly of SGs

While ubiquitin and SUMO conjugation emerge as important regulators of SG dynamics, the role of NEDD8 in this process has been controversial (*40*, *41*). Long-term inhibition (15 hours) of the NEDD8 pathway reduced SG assembly induced by arsenite, whereas no effect on SG dynamics was observed upon short-term inhibition (1 to 2 hours). A possible explanation for these differences is that short-term inhibition of the NEDD8 pathway may not provide a complete deNEDDylation of substrates in contrast to long-term inhibition (*32*). To better understand the implication of NEDDylation in the regulation of SG dynamics, we focused on the deNEDDylating enzyme NEDP1, which is a critical and highly specific component of the NEDD8 cycle that deconjugates NEDD8 mainly from non-cullin substrates (*32*). The study of NEDP1 provides a highly specific approach to decipher the role of protein NEDDylation in SG dynamics.

We generated cell lines stably expressing green fluorescent protein (GFP)–G3BP1, the nucleator of SGs, in parental or NEDP1 KO U2OS cells (*50*, *51*). Exposure of cells to arsenite caused an accumulation of NEDD8 conjugates (Fig. 1A and fig. S1A). The observed increase in NEDD8 modification strictly depends on the NAE and not on the ubiquitin system, which can activate and conjugate NEDD8 on substrate proteins under stress conditions, including heat shock or proteasome inhibition (fig. S1B) (*52*). NEDP1 KO causes an increase in protein NEDDylation, and no further increase was observed upon arsenite treatment (Fig. 1A and fig. S1A). The response is reversible, as stress alleviation results in a progressive decrease in the levels of NEDD8 conjugates induced upon stress, indicative of a recovery process (Fig. 1B). The data indicate that the NEDD8 pathway is part of the arsenite stress response. Under these conditions, we found by imaging on GFP-G3BP1 cells (Fig. 1, C and D) and on endogenous TIA1 (fig. S1C) that NEDP1 KO accelerates both the formation and elimination of SGs. Similar results were obtained using heat shock as another inducer of SG formation (fig. S1D). We found that the effect of NEDP1 KO on SG dynamics is not due to changes in the levels of SG proteins (fig. S1E) but due to the increase in protein NEDDylation, as inhibition of the NEDD8 pathway with the inhibitor of NAE (NAEi; MLN4924) reversed the NEDP1 phenotype in SG disassembly (Fig. 1E). In addition, we assessed the effect of transient inhibition of NEDP1 on SG dynamics. For this, we transiently expressed an anti-NEDP1 Nb (Nb9) that displays nanomolar binding affinity and specifically inhibits NEDP1 activity (*53*). Characterization in vitro and in tissue culture cells shows that Nb9 potently inhibits the deconjugating activity of NEDP1, resulting in the accumulation of NEDD8 conjugates (*53*). Consistent with this notion, expression of Nb9 increases protein NEDDylation and accelerates SG assembly/disassembly, similarly to what is observed upon NEDP1 KO (Fig. 1, F to H). The role of NEDP1 in SG elimination depends on its catalytic activity, as expression of wild type, but not of the catalytic NEDP1 Cys mutant (C163A), reduced the rate of SG disassembly in NEDP1 KO cells (fig. S1, F and G).

To better define the role of NEDP1 in SG dynamics, we monitored the size and number of SGs formed upon arsenite using either the GFP-G3BP1 cells (Fig. 2, A to E) or monitoring endogenous TIA1 as SG marker (fig. S2, A to C). We found that NEDP1 KO

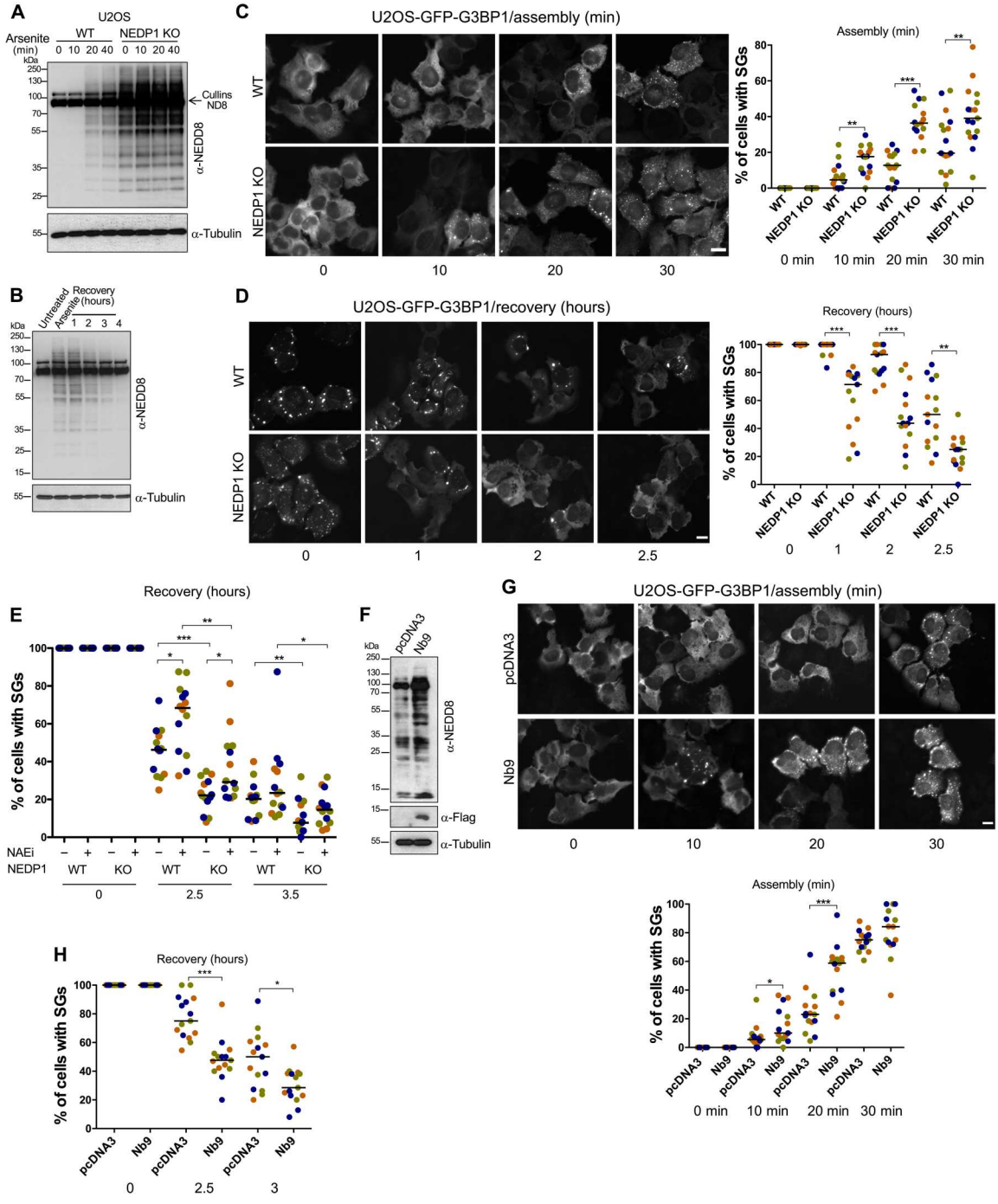

Fig. 1. NEDP1 inhibition accelerates the formation and elimination of SGs. (**A**) Parental and NEDP1 KO U2OS cells were treated with sodium arsenite (arsenite) (0.5 mM), and lysates were analyzed by Western blotting with the indicated antibodies. (**B**) U2OS cells were treated with arsenite and allowed to recover for the indicated periods. Extracts were used for Western blotting as in (A). (**C**) Parental and NEDP1 KO U2OS cells stably expressing GFP-G3BP1 were treated with arsenite and then fixed at indicated time points. Scale bars, 10 μm. Right: Quantification of the experiment performed in (C) showing the percentage of cells with SGs. Each dot represents a separate field analyzed (20 to 25 cells), and each color represents an independent experiment ($n = 3$). (**D**) Cells were treated with arsenite (1 hour that provides almost 100% of cells with SGs) before they were allowed to recover for the indicated periods. Right: Quantification of the experiment in (D) displaying the percentage of cells with SGs during recovery. Each dot represents a separate field analyzed (20 to 25 cells), and each color represents an independent experiment ($n = 3$). (**E**) Parental and NEDP1 KO U2OS cells stably expressing GFP-G3BP1 were pretreated with 0.5 μM NAEi (4 hours) and then treated for 1 hour with arsenite, washed with PBS, and then incubated in fresh medium containing 0.5 μM NAEi for the indicated periods before fixation. Graph represents the percentage of cells with SGs as described above ($n = 3$). (**F**) U2OS cells were transfected with empty (pcDNA3) or Nb9-Flag–expressing constructs (2 μg). Extracts were analyzed by Western blotting using the indicated antibodies. (**G**) Similar experiment as in (C), except that U2OS cells were transfected with empty (pcDNA3) or Nb9-Flag–expressing constructs. Bottom: Quantification of the experiment performed in (G) presented as above ($n = 3$). (**H**) Experiment performed as in (D) except that U2OS cells were transfected with empty (pcDNA3) or Nb9-Flag–expressing constructs ($n = 3$).

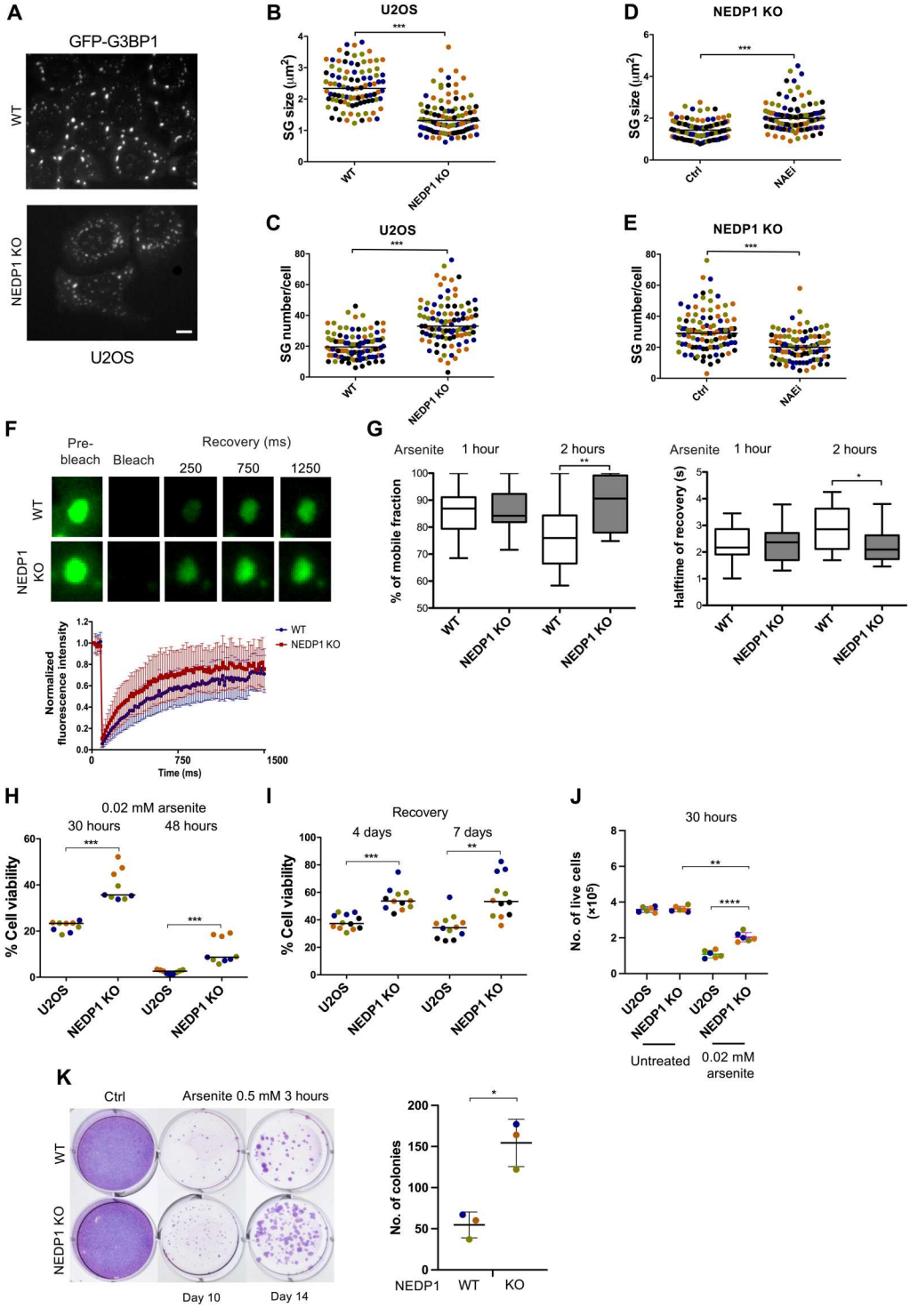

Fig. 2. NEDP1 inhibition decreases SG size, maintains the mobility of SG proteins, and protects cells against stress. (**A**) SG assembly was monitored by video microscopy in parental or NEDP1 KO U2OS cells stably expressing GFP-G3BP1 treated with 0.2 mM arsenite (image after 1 hour of treatment; movies S1 and S2). Scale bar, 10 μm. Plots showing the size (**B**) and number per cell (**C**) of SGs in ~25 cells per condition (mean ± SD). Each dot represents an individual SG/cell, and each color represents an independent experiment ($n = 4$). (**D** and **E**) Experiment as in (A), except that NEDP1 KO cells were pretreated with 0.5 μM NAEi (4 hours) before treatment with arsenite (1 hour). Plots showing SG size and SG number per cell in ~25 cells. (**F**) Parental or NEDP1 KO U2OS stably expressing GFP-G3BP1 cells were treated with 0.2 mM arsenite and analyzed by FRAP as described in Materials and Methods (four cells per experiment, $n = 2$, 5 to 7 SGs per cell analyzed). Images for the bleach and recovery period are shown. The graph represents the normalized fluorescence intensity of one of the performed experiments. (**G**) The mobile fraction (left) and halftime recovery (right) are presented for the indicated period of arsenite treatment (mean ± SD from the two experiments). (**H**) Parental and NEDP1 KO U2OS cells were plated in 96-well plates and treated continuously with 0.02 mM arsenite for 30 or 48 hours before viability was measured with the CellTiter-Glo assay. (**I**) Experiment as in (H), except cells were treated with arsenite (0.5 mM) for 1 hour and allowed to recover for the indicated period where cell viability was measured. (**J**) Experiment was performed as in (H), and the number of live cells was counted as described in Materials and Methods. Each dot represents a replicate experiment, and each color represents an independent experiment ($n = 3$ to 4). (**K**) Clonogenic assays in parental and NEDP1 KO U2OS cells treated with arsenite. Graph represents the number of colonies in each experiment (mean ± SD, $n = 3$).

reduces the size and increases the number of formed SGs upon arsenite (Fig. 2, A to C, and movies S1 and S2), and these effects were reversed upon inhibition of the NEDD8 pathway (Fig. 2, D and E).

In addition, we excluded the possibility that the observed NEDP1 phenotype on SGs is due to defects in microtubule dynamics. Microtubules are proposed to assist growth of SGs through transport and fusion of smaller SGs, and similarly to NEDP1 inhibition, microtubule disruption results in the formation of smaller and more numerous SGs (*54*). By measuring in real time different parameters of microtubule dynamics such as the growth speed, length, and lifetime of microtubule tracks, we found no differences between parental and NEDP1 KO cells (fig. S2, D to F, and movies S3 and S4). Collectively, the experiments strongly suggest that inhibition of NEDP1 activity accelerates both the formation

and elimination of SGs through an increase in protein NEDDylation.

NEDP1 inhibition increases the mobility of SG proteins and protects cells against stress-induced toxicity

A biophysical property that defines the dynamicity and is directly related to the potential pathogenicity of SGs is the mobility of SG proteins within the condensates. Prolonged stress conditions reduce protein mobility within SGs, leading to their transition from a liquid-liquid into a liquid-solid phase that compromises SG elimination during the recovery period (*16*, *22*). By fluorescence recovery after photobleaching (FRAP), we found that prolonged exposure of parental cells to arsenite reduced the mobility of GFP-G3BP1 protein with concomitant increase in the half-life of recovery (Fig. 2, F and G). In contrast, in NEDP1 KO cells, both the mobility and half-life recovery were unaffected by arsenite (Fig. 2, F and G), suggesting that NEDP1 inhibition prevents the transition of SGs into a liquid-solid phase by maintaining the mobility of SG proteins. In addition, in survival/clonogenic assays, NEDP1 KO protects cells against the induced toxicity by arsenite (Fig. 2, H to K). The data suggest that NEDP1 inhibition promotes SG disassembly by maintaining the mobility of SG proteins, which is correlated to protection of cells against stress-induced toxicity.

NEDP1 controls SG dynamics through deNEDDylation of PARP-1

To reveal mechanisms for the role of NEDP1 in the control of SG dynamics, we sought to define NEDP1 substrates. Previous proteomic studies identified hundreds of potential substrates for NEDP1; however, these results were based on the use of a NEDD8 mutant (R74K), which may alter the biochemical properties of NEDD8 (*55*, *56*). We developed a strategy that allows the identification of NEDP1-dependent NEDDylation sites under endogenous expression of wild-type NEDD8. We combined the use of anti-diGly antibodies that recognize both ubiquitin and NEDD8-modified peptides upon trypsin digestion with short treatment of cells with the ubiquitin E1 inhibitor MLN7243 (UAEi), which markedly reduces ubiquitin, but not NEDD8 modification (fig. S3A). We hypothesized that by eliminating most of the ubiquitin-derived diGly peptides upon MLN7243 treatment, we would be able to quantify NEDP1-dependent diGly peptides (Fig. 3A). We previously established the HCT116 colorectal cells as model system for the identification of NEDDylation sites using the diGly approach (*55*). Extracts from parental and NEDP1 KO HCT116 cells both treated with UAEi were used for the isolation of diGly-modified peptides and mass spectrometry (MS) analysis (Fig. 3A). We quantified changes in the abundance of 2897 unique modified peptides on 1206 unique proteins between control and NEDP1 KO cells and found 934 peptides from 568 proteins and 424 peptides from 328 proteins for which at least a twofold increase or decrease, respectively, was detected upon NEDP1 KO (data S1). The coordinated action of conjugating and deconjugating enzymes such as NEDP1 ensures NEDD8 recycling, preserving the so-called free pool of NEDD8. The observed decrease in NEDDylation upon NEDP1 KO is most likely an indirect consequence of blocking the release and recycling of NEDD8 into the free pool. The decrease in free NEDD8 available for conjugation would subsequently reduce the NEDDylation of substrates that are regulated by other deconjugating enzymes than NEDP1. Thus, the observed decrease probably indicates NEDDylation events that are not directly controlled by NEDP1 (*32*). In contrast, increase in NEDDylation indicates proteins that are direct NEDP1 substrates.

By comparing our dataset with previous proteomic analysis that defined the SG proteome (*37*), we found as potential NEDP1-dependent NEDD8 substrates several SG proteins, such as the core protein G3BP1; translation initiation factors EIF4A1, EIF3D, EIF3E, EIF3I, and EIF3L; and ribonucleoproteins HNRNPA1, HNRNPD, HNRNPH1, and HNRNPK (fig. S3B and data S2). This is consistent with the previously proposed idea that the NEDD8 pathway may directly control SG biology through modification of SG proteins (*40*). Among the target proteins, we identified PARP-1, which attracted our attention for the following reasons: First, PARP-1 is a critical regulator of SG dynamics, as PARylation, including of several SGs proteins, generates a scaffold for protein-protein and RNA interactions that is required for SG assembly (*49*). Second, previous studies indicated that NEDP1 regulates PARP-1 activity upon oxidative stress (*46*). Third, high-confidence NEDDylation sites on PARP-1 that depend on NEDP1 were reported in all previous NEDD8 proteomic studies and also identified in our studies (*55*, *56*) (Fig. 3B and data S1). Last, in an "epistasis-like" experiment, we monitored the effect of PARP-1 inhibition on SG formation and disassembly in control and NEDP1 KO cells. Chemical inhibition of PARP-1 with olaparib (fig. S3C) causes the generation of smaller and more numerous SGs (fig. S3, D and E) and accelerates their disassembly compared to control untreated cells (fig. S3F), similarly to what is observed upon NEDP1 KO. However, PARP-1 inhibition had no significant effect either on SG size/number or rates of SG disassembly in NEDP1 KO cells, strongly suggesting that NEDP1 and PARP-1 are functionally linked for the formation/disassembly of SGs (fig. S3, D to F).

We first determined whether PARP-1 is a NEDP1-dependent NEDD8 substrate. We isolated NEDD8 conjugates from control and NEDP1 KO human embryonic kidney (HEK) 293 cells stably expressing His_6-NEDD8 and monitored the NEDDylation of endogenous PARP-1 by Nickel pull-down (Nickel-PD) and Western blotting (Fig. 3C). NEDP1 KO increases PARP-1 NEDDylation (Fig. 3C). In a reverse experiment using instead overexpression of His_6-PARP-1 and Nickel-PD, we found that NEDP1 KO increases the modification of PARP-1 with endogenous NEDD8 (Fig. 3D). Similar observations were obtained upon transient inhibition of NEDP1 with Nb9 (Fig. 3E). Exposure of cells to arsenite did not have a significant effect on PARP-1 NEDDylation in NEDP1 KO cells (Fig. 3, C and D), which was, however, reduced upon treatment with the NAE inhibitor MLN4924 (Fig. 3D, NAEi).

Our current and previous proteomic studies identified the following potential NEDP1-dependent NEDDylation sites on PARP-1: K425 (Fig. 3B and data S1), K364, K518, and K637 (*55*, *56*). To characterize the role of PARP-1 NEDDylation in SG dynamics, we mutated these lysine residues on PARP-1 into arginine (R). Wild-type and mutant His_6-PARP-1 constructs were expressed in control and NEDP1 KO HEK293 cells, and their modification with endogenous NEDD8 was monitored upon isolation of His_6-PARP-1 by Nickel-PD as before (Fig. 3F). We found that mutation of K425, K518, and K637 into arginine or the generation of a double mutant (K518/637R, KDMR) significantly, but not completely, reduced PARP-1 NEDDylation (Fig. 3, F and G). No effect was observed upon mutation in K346, which intriguingly altered the migration profile of PARP-1 (Fig. 3, F and G). Mutation of all four

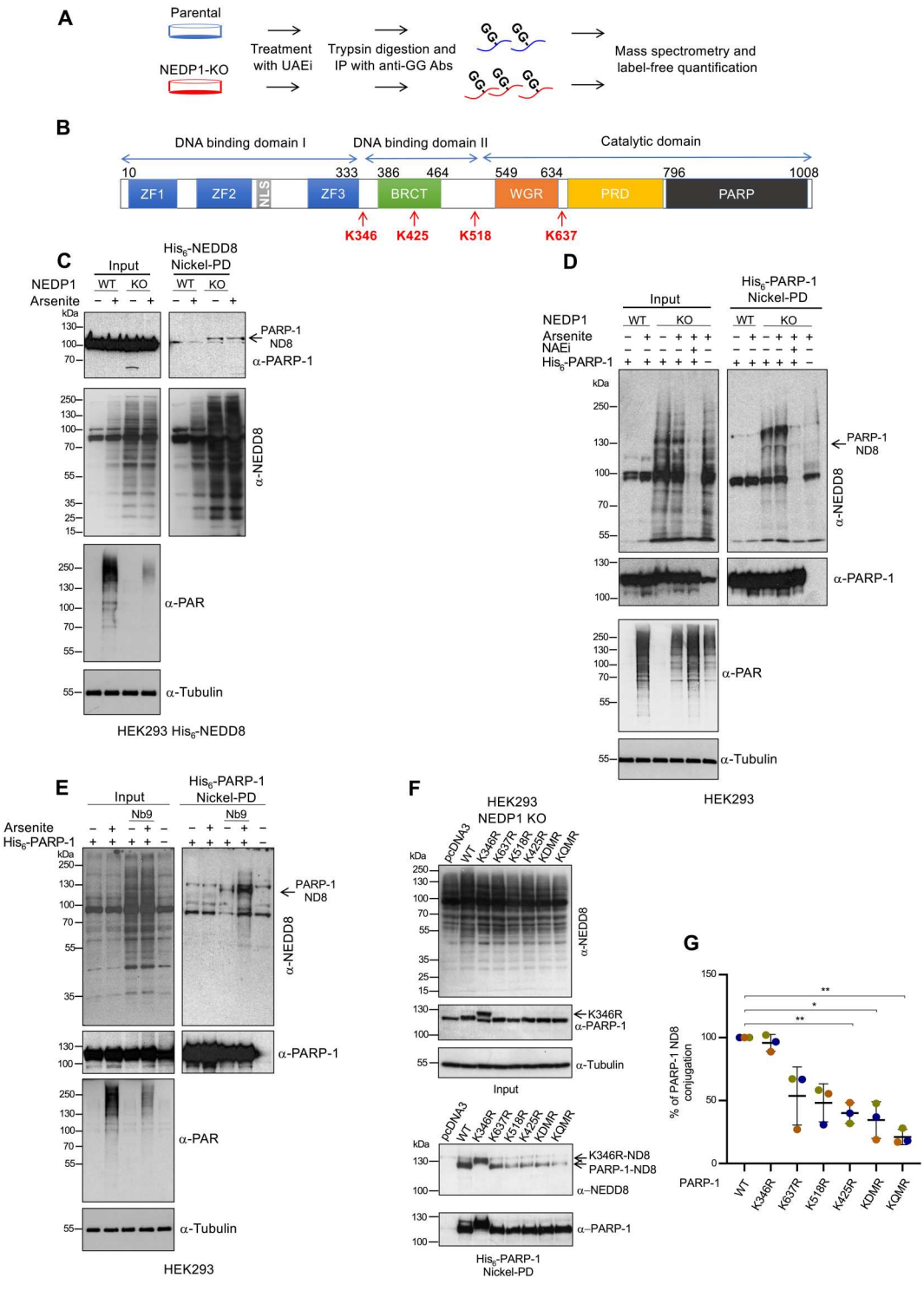

Fig. 3. PARP-1 is a NEDD8 substrate for NEDP1. (**A**) Schematic representation of the proteomic approach to identify NEDDylation sites controlled by NEDP1 at endogenous levels of wild-type NEDD8 expression. Parental and NEDP1 KO HCT116 cells were treated with UAEi (0.5 μM, 5 hours) before extracts were used for trypsin digestion and immunoprecipitations with anti-diglycine antibodies and mass spectrometry analysis. Data were used for label-free quantification. (**B**) Schematic representation of PARP-1 domains including the identified NEDDylated lysine residues upon NEDP1 KO in current (K425) and previous studies (*55*, *56*). (**C**) Parental and NEDP1 KO HEK293 cells stably expressing His_6-NEDD8 were treated with arsenite (0.5 mM, 1 hour) before extracts were used for Nickel-PD. Isolated His_6-NEDD8 conjugates and total cell extracts (input) were used for Western blot analysis with the indicated antibodies. (**D**) Parental and NEDP1 KO cells were transfected with His_6-PARP-1. Forty-eight hours after transfection, cells were treated with arsenite (0.5 mM, 1 hour) as indicated, and extracts were used for Nickel-PD and Western blot analysis as in (C). (**E**) HEK293 cells were transfected with His_6-PARP-1 and Nb9-expressing constructs as indicated. Forty-eight after transfection, cells were treated with arsenite (0.5 mM, 1 hour) and Nickel-PD and Western blot analysis was performed as in (D). (**F**) NEDP1 KO HEK293 cells were transfected with the indicated His_6-PARP-1–expressing constructs and, 48 hours later, were used for Nickel-PD. Isolated proteins and total cell extracts (input) were used for Western blot analysis as indicated. (**G**) Quantification of the experiment performed in (F) (His_6-PARP-1 Nickel-PD). The relative level of NEDDylation of PARP-1 mutants compared to wild type (WT) is presented. Values represent the mean ± SD, $n = 3$.

lysines into arginine (quadruple mutant, KQMR) caused the most profound reduction in PARP-1 NEDDylation (Fig. 3, F and G). The detection of a single band as a major modified PARP-1 species may be due to the simultaneous conjugation of PARP-1 with multiple NEDD8 molecules at different sites or due to the presence of distinct pools of PARP-1 that each is modified with a single NEDD8 molecule at different sites. The analysis indicates that multiple sites in PARP-1 are used for NEDDylation, with K425 and K518 as the most prominent.

To assess the potential role of PARP-1 NEDDylation in SG dynamics, we used the KQMR and the single K425R mutant as they displayed the most reproducible reduction in PARP-1 NEDDylation (Fig. 3G). These mutants were expressed in PARP-1 KO U2OS (*57*) and PARP-1/NEDP1 double KO cells generated by

CRISPR-Cas9 (*45*) to avoid any interference from the expression of endogenous PARP-1. Expression of either of the two NEDDylation defective PARP-1 mutants resulted in higher levels of PAR upon arsenite treatment compared to wild-type PARP-1, indicating that NEDDylation reduces PARP-1 activity (Fig. 4A and fig. S4A). Consistent with this notion, the levels of PAR induced upon arsenite are lower in NEDP1 KO or Nb9-expressing cells compared to parental/control cells (Figs. 3, C to E, and 4B). The use of several DNA damage inducers that are known to activate PARP-1 showed that NEDP1 KO reduces PAR production upon methyl methanesulfonate (MMS), but not upon camptothecin (CPT), etoposide, or ultraviolet-C (UV-C) treatment (fig. S4B). This indicates that the role of NEDP1 in PARP-1 activity control is stress specific.

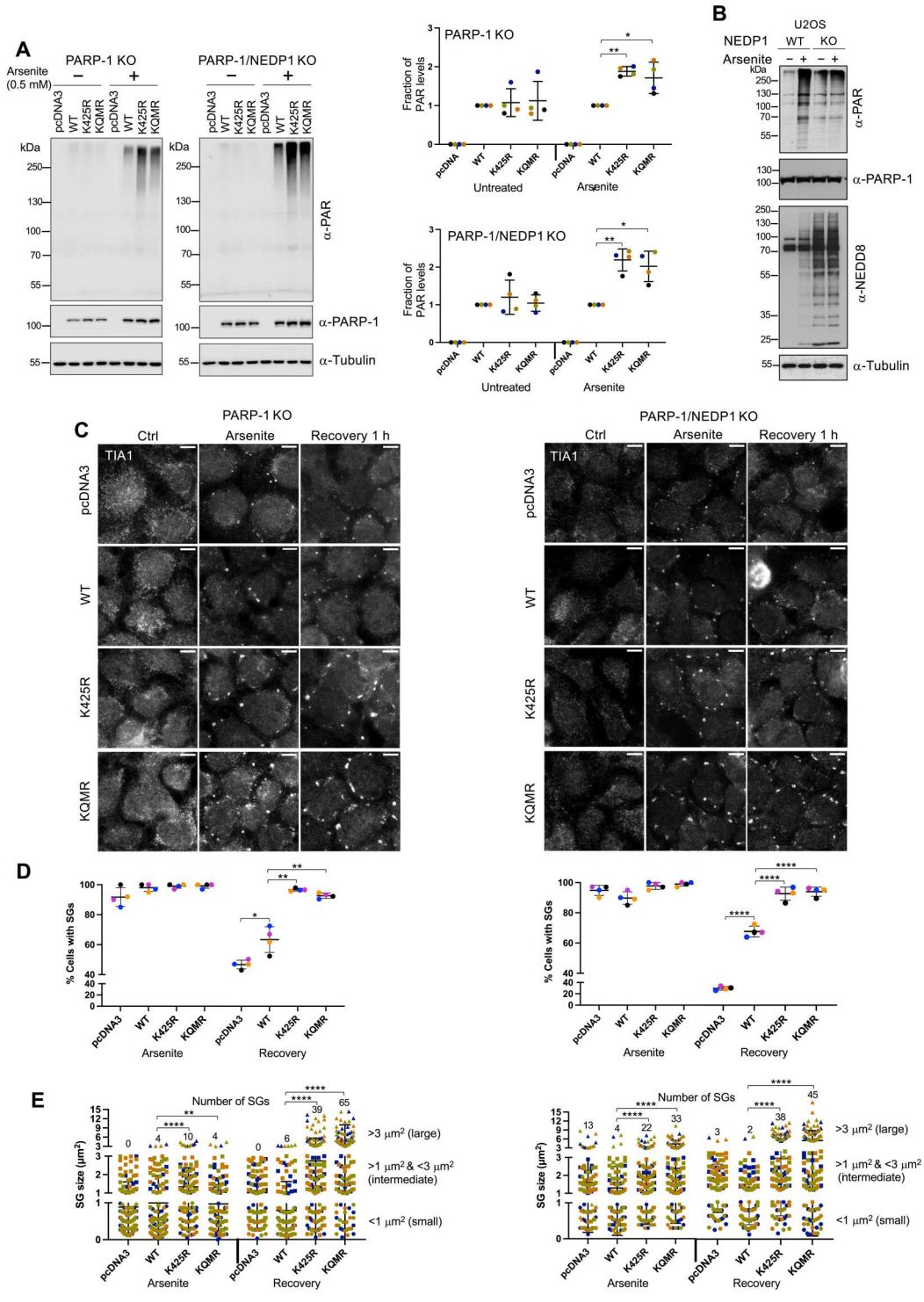

Fig. 4. PARP-1 NEDDylation inhibits PARP-1 activity and is responsible for the NEDP1 phenotype for SG size and disassembly. (**A**) Left: PARP-1 KO and PARP-1/NEDP1 double KO U2OS cells were transfected with the indicated plasmids expressing WT or NEDDylation-deficient PARP-1 mutants. Forty-eight hours after transfection, cells were either untreated or treated with arsenite (0.5 mM, 1 hour) and total cell extracts were used for Western blot analysis with the indicated antibodies. Right: Quantification of the experiment on the left. Values represent the mean ± SD, $n = 4$ of the fraction of PAR production (WT was used as the reference for each condition). (**B**) Parental or NEDP1 KO U2OS cells were treated with arsenite (0.5 mM, 1 hour), and extracts were used for Western blot analysis with the indicated antibodies. (**C**) Experiment was performed as in (A), except that recovery was also monitored as indicated. Formation of SGs was monitored by immunostaining for endogenous TIA1. (**D**) In the experiment performed in (C), the percentage of cells with SGs is shown. Each dot represents an independent experiment ($n = 4$, ~100 cells per condition). The mean value ± SD is also presented. (**E**) In the experiment performed in (C), the size of SGs was measured. Each dot represents an individual SG, each shape represents a different size of SG, and each color represents an independent experiment ($n = 3$, 50 cells per condition per experiment). The total number of SGs with size of >3 μm^2 (large) for each condition is also indicated.

We next monitored the effect of wild-type and mutant PARP-1 expression in SG dynamics using endogenous TIA1 as SG marker. Compared to parental U2OS, PARP-1 KO cells produce smaller SGs upon arsenite, consistent with the important role of PARP-1 in SG formation (fig. S4C). Using PARP-1 KO U2OS cells, we found that SG disassembly was delayed in cells expressing the PARP-1 mutants, compared to cells expressing wild-type PARP-1 (Fig. 4, C and D). In addition, under these conditions, the expression of the PARP-1 mutants is correlated with an increase in the size of SGs, especially during the recovery period (Fig. 4, C and E). Collectively, the data support the following hypothesis: NEDP1 inhibition causes the hyper-NEDDylation of PARP-1, which reduces PAR production. This results in the formation of smaller SGs, which are disassembled faster during the recovery period compared to control cells (fig. S4D).

NEDP1 inhibition accelerates the disassembly of SGs containing mutated proteins associated with ALS

Mutations in many SG proteins in ALS are related to the formation of aberrant SGs. A key characteristic of these inclusions is their persistence in the cytoplasm compared to the relative fast elimination of physiological SGs during recovery (*18*). NEDP1 KO or inhibition by Nb9 accelerated the disassembly of SGs containing well-established ALS-derived mutants for TIA1 (A381T and E384K) (*18*), which are disassembled slower compared to SGs containing wild-type TIA1 (Fig. 5, A to C). We next assessed whether NEDP1 inhibition promotes the elimination of aberrant SGs using more physiologically relevant in vitro systems. To this end, transfection of mouse-derived hippocampal neurons with Nb9 accelerated the elimination of both wild-type and mutant GFP-TIA1 SGs, similarly to what is observed in transformed cells (Fig. 5D). In addition, we determined the effect of NEDP1 inhibition on SG elimination in skin fibroblasts derived from a patient affected by sporadic ALS (sALS; 37/15). These fibroblasts were previously compared to several fibroblasts derived from independent healthy donors, showing that in these sALS cells the elimination of SGs is severely delayed (*19*). Consistent with these studies, we found that the elimination of SGs (eIF4G1 staining) during the recovery period is significantly delayed in ALS 37/15 fibroblasts, compared to the control HDF20 fibroblasts obtained from a healthy donor (fig. S5A). To achieve high level of NEDP1 inhibition in these cells, we used infection with retrovirus expressing Nb9 that accelerated the elimination of SGs in both healthy HDF20 and sALS 37/15 fibroblasts compared to control cells (fig. S5A). Using an empty viral vector as a control, we excluded that viral infection per se influences SG dynamics (fig. S5B). While we cannot generalize the effect of NEDP1 inhibition on SG dynamics to other patient-derived fibroblasts, collectively, the data reveal that NEDP1 inhibition accelerates the clearance of aberrant SGs in several tested in vitro systems.

nedp1 deletion promotes the clearance of aberrant SGs and restores motility in the *sod-1*^{G85R} and *C9orf72* G4C2 expansion *C. elegans* ALS models

To assess the role of NEDP1 on SG formation at the organism level, we used the worm *C. elegans* as an established model for neurodegenerative diseases, including ALS. A well-established *C. elegans* ALS model is based on the introduction of the human ALS-linked SOD1 mutation G85R in the worm homologous gene *sod-1*. This leads to a strong motility defect associated with the presence of insoluble aggregates of the SOD1 G85R protein, recapitulating an ALS-related cellular defect (*58*, *59*). Exposure of wild-type animals expressing endogenous GFP-tagged *gtbp-1* (worm homolog of G3BP-1) as SG marker (*60*) to acute (arsenite), prolonged (15 hours, paraquat) oxidative stress or heat shock induced the formation of GTBP-1 protein puncta, indicative of SG formation in muscle pharyngeal cells (Fig. 6, A and B, and fig. S6A). Similar experiments in *gtbp-1::gfp* animals expressing the SOD1 G85R mutant (*sod-1*^{G85R}) showed that upon arsenite treatment, larger GTBP-1-GFP SGs were generated compared to control animals (Fig. 6, A and B, and fig. S6B). The phenotype on SG size in the SOD1 mutant animals was even more profound upon prolonged oxidative stress (15 hours, paraquat) (fig. S6A). The data are consistent with the formation of aberrant inclusions in the muscle pharyngeal cells and presumably in the surrounding neurons in the *sod-1*^{G85R} mutant. Strikingly, under all applied stress conditions, deletion of *ulp-3* (worm homolog of *nedp1*) (*45*) reduced the formation of GTBP-1-GFP SGs both in wild-type and in the *sod-1*^{G85R} mutant background (Fig. 6, A and B, and fig. S6, A and B). In addition to the *sod-1*^{G85R} mutant, we also tested the effect of *ulp-3* deletion on the *C. elegans C9orf72* expansion (C9) ALS model (*61*). These animals carry 75 copies of the hexanucleotide repeat expansion GGGGCC (G4C2), normally found in the *C9orf72* human gene, representing the most frequent genetic abnormality of inherited ALS/FTD (*62*, *63*). The G4C2 repeats are flanked by intronic sequences found upstream or downstream of the G4C2 repeats within the human *C9orf72* gene and are under the control of a ubiquitous promoter. Expression of these repeats results in the formation of RNA foci and production of dipeptide repeat proteins that are established to cause proteotoxicity (*61*, *64*). As these animals carry a GFP-myo-2 marker for the presence of the G4C2 expansion (fig. S7), we generated C9 animals that express a red fluorescent protein (RFP) version of GTBP-1 as SG marker. Exposure of the C9 animals to arsenite causes the accumulation of large SGs compared to wild-type animals, indicative of the generation of aberrant SGs (Fig. 7, A and B). Similarly to what is observed in the *sod-1*^{G85R} mutant animals, deletion of *ulp-3* reduces the number and the size of aberrant SGs in the C9 background (Fig. 7, A and B). The analysis in human cells and in *C. elegans* revealed a highly conserved role for NEDP1/ULP-3 in the elimination of physiological and pathological ALS-related SGs.

To assess the potential functional link between aberrant SG elimination and ALS-related pathology, we examined the effect of *sod-1*^{G85R} mutation and G4C2 expansion on worm locomotion (CeleST) (*65*) and the impact of *ulp-3* deletion. By measuring two different parameters of animal motility (wave initiation rate and the activity index), we found that the *sod-1*^{G85R} mutants showed a clear defect in locomotion compared to the wild-type animals. This phenotype was even more severe in the C9 animals (Fig. 8, A and B, and movies S5, S6, S9, and S10). Deletion of *ulp-3* has no significant effect in animal motility in control animals (Fig. 8A and movie S7). However, *ulp-3* deletion almost completely restored the observed phenotypic defects to wild-type levels in the *sod-1*^{G85R} mutant, whereas a partial rescue was observed in the C9 animals (Fig. 8, A and B, and movies S8 and S11). This difference may reflect the pleiotropic role of G4C2 expansion in ALS pathology, where formation of aberrant SGs is one of the multiple imposed defects (*64*, *66*). Overall, the data suggest that the elimination of ALS-related SGs observed in the *sod-1*^{G85R} mutant and C9

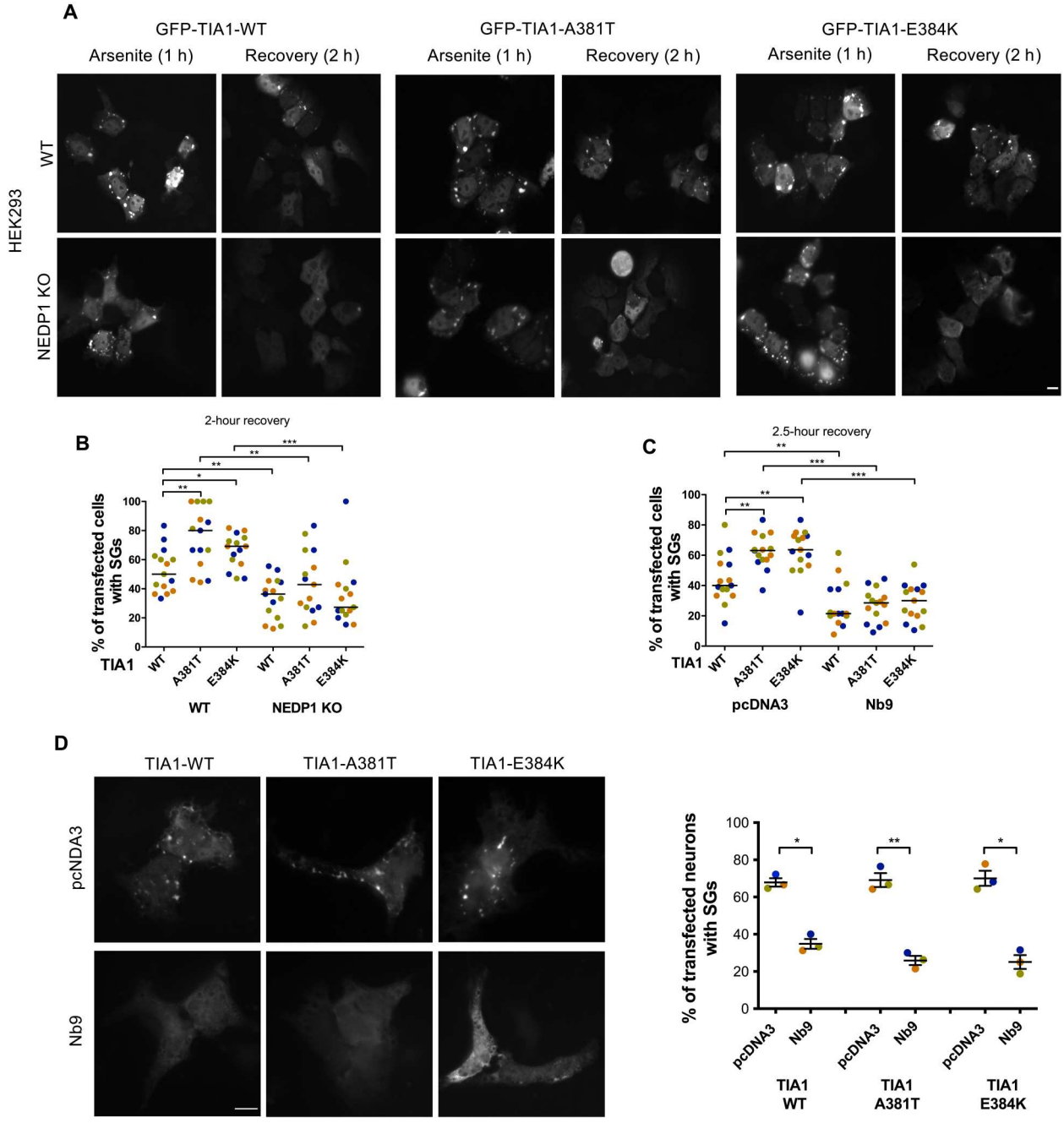

Fig. 5. NEDP1 inhibition accelerates the elimination of SGs containing ALS-related mutant proteins. (**A**) Parental and NEDP1 KO HEK293 cells were transfected with the indicated GFP-TIA1 constructs (1 μg), and 48 hours after transfection, cells were stressed with arsenite (0.5 mM, 1 hour) before recovery (2 hours). SG formation was monitored by GFP fluorescence. (**B**) Quantification of the experiment performed in (A). Each dot represents a separate field analyzed (20 to 25 cells), and each color represents an independent experiment ($n = 3$). The mean value is also indicated. (**C**) Experiment performed as in (A), except that, where indicated, the Nb9 expression construct was cotransfected. Quantification was performed as in (B). (**D**) Mouse-derived hippocampal neurons were transfected with the indicated GFP-TIA1 and Nb9 constructs, stressed with arsenite (0.2 mM, 1 hour), before they were allowed to recover for 2 hours. SG formation was monitored by GFP fluorescence. Each dot in the right panel represents the percentage of cotransfected neurons with SGs during recovery from an independent experiment ($n = 3$, 20 to 25 cotransfected neurons per condition). Scale bar, 10 μm.

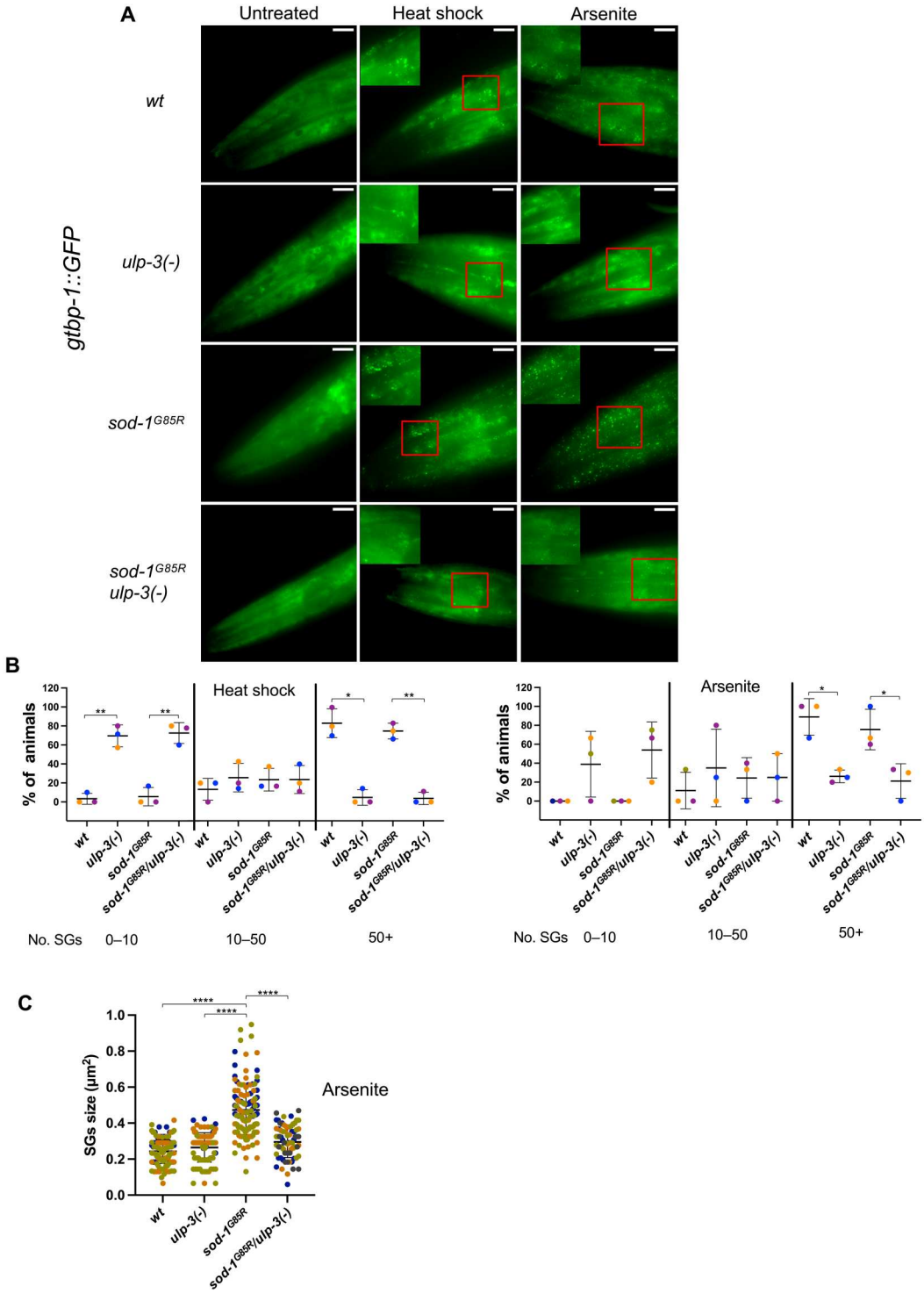

Fig. 6. Deletion of *ulp-3* (*nedp1*) decreases the number of SGs in the *C. elegans sod-1*^{G85R} ALS model system. (**A**) Animals expressing GTBP-1-GFP on the indicated genetic backgrounds were either untreated or exposed to heat shock or arsenite, as described in Materials and Methods. The formation of SGs was monitored by GFP fluorescence. (**B**) Quantification of the experiment performed in (A), representing the percentage of animals with the indicated number of SGs. Each color represents an independent experiment (n = 3, 10 animals per experiment). The mean values ± SD are also presented. (**C**) Quantification of the size of SGs upon arsenite treatment. Each dot represents an individual SG and each color an independent experiment (n = 3, five animals per condition per experiment).

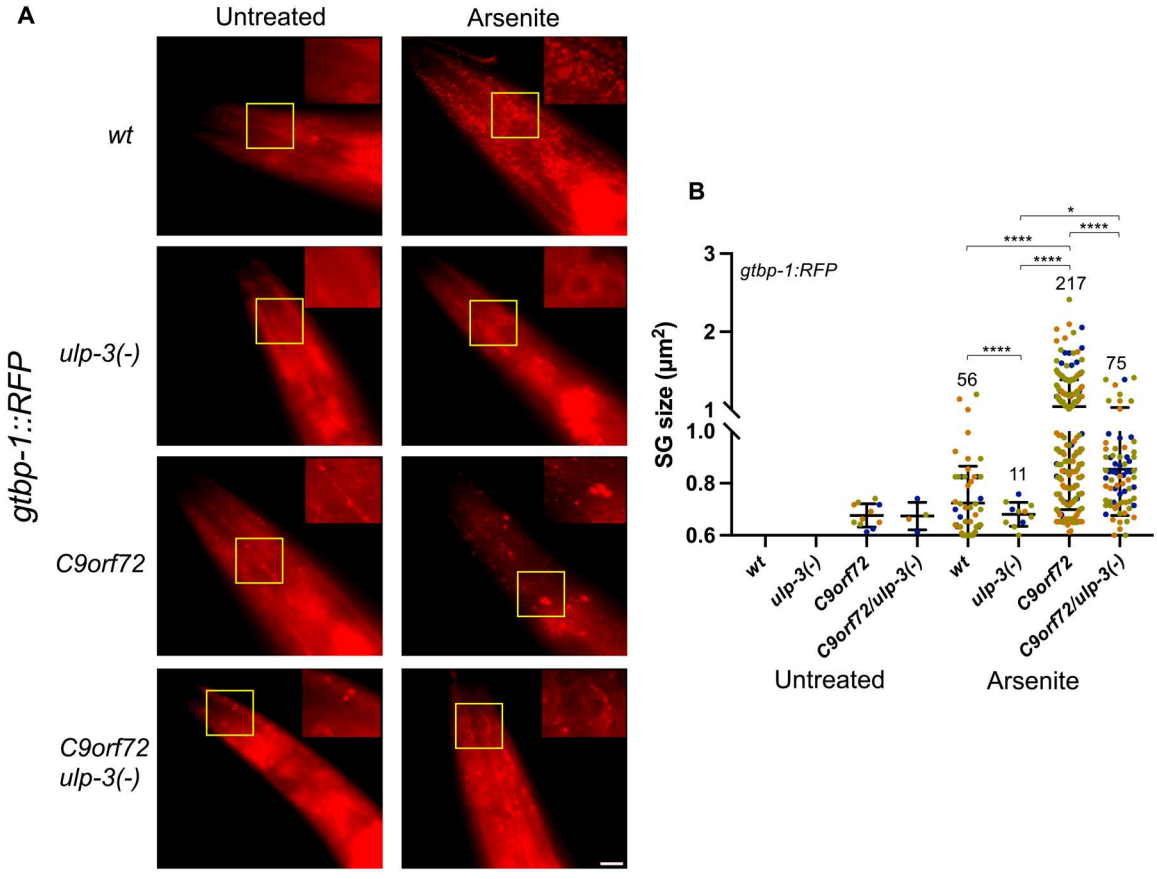

Fig. 7. Deletion of *ulp-3* (*nedp1*) decreases the number of SGs in the *C. elegans C9orf72* ALS model system. (**A**) Animals expressing GTBP-1-RFP on the indicated genetic backgrounds were either untreated or exposed to arsenite as described in Materials and Methods. The formation of SGs was monitored by RFP fluorescence. (**B**) Quantification of the size of SGs. Each dot represents an individual SG with size of >0.6 μm^2 (considered as large SGs), and each color represents an independent experiment (n = 3, five animals per condition per experiment). The total number of SGs with size of >0.6 μm^2 is shown.

animals upon *ulp-3* deletion is correlated with the rescue of ALS phenotypes related to animal motility.

DISCUSSION

The formation of SGs is induced by a broad range of stress stimuli and is regarded as a protective mechanism to a broad range of stress stimuli (*9*). The assembly and disassembly processes collectively characterize the dynamic nature of SGs, which is the essence of their protective role upon stress (*9*, *11*, *67*). The generation and persistence of aberrant inclusions due to mutations in several genes encoding for SG proteins is regarded as hallmark in neurodegenerative diseases, such as ALS/FTD (*14*, *15*, *17*). However, how alterations in SG dynamics contribute to the formation of the toxic protein inclusions and the impact of aberrant SGs in the onset/progression of ALS/FTD is still unclear (*22*, *23*). The definition of pathways and development of approaches that promote the elimination of aberrant SGs would allow to assess their role in pathology. Consistent with this notion, inhibition of NEDP1 accelerates the disassembly of SGs containing either wild-type or ALS-derived mutant SG proteins and is correlated with amelioration of ALS-related defects. Detailed kinetic analysis revealed that inhibition of NEDP1 accelerates both SG assembly and disassembly. The formation and dissolution of SGs are regarded as multistep events. The initial formation of the core is followed by the progressive recruitment of the shell proteins and/or by fusion events that result in the growth of SGs (*11*, *68*). Whether these steps in SG assembly follow the same rates is not clear. On the basis of the observation that NEDP1 KO cells produce higher number of smaller SGs compared to wild-type cells, the apparent acceleration in SG assembly may reflect a defect in the subsequent growth/fusion of SGs. How an increase in the mobility of SGs (observed upon NEDP1 inhibition) would control SG growth/fusion and/or disassembly is currently unclear. The observed changes in SG size and mobility upon NEDP1 inhibition may in turn be the basis of the accelerated SG dissolution observed during the recovery process. As NEDP1 also controls the dynamics of aberrant SGs, the above-described characteristics indicate a fundamental function of NEDP1 in SG biology.

Previous studies identified the splicing regulator SRSF3, which is localized within SGs upon arsenite treatment, as a NEDD8 substrate. The studies indicated that modification of SRSF3 in K85 is required for SG formation (*40*). While SRSF3 was not identified as a NEDP1-dependent NEDD8 target in our proteomic analysis, several reported SG proteins including splicing factors were found (e.g., SF3B2 and HNRNP ribonucleoproteins; fig. S3B and data S2). Although these data suggest that modification of SG proteins with

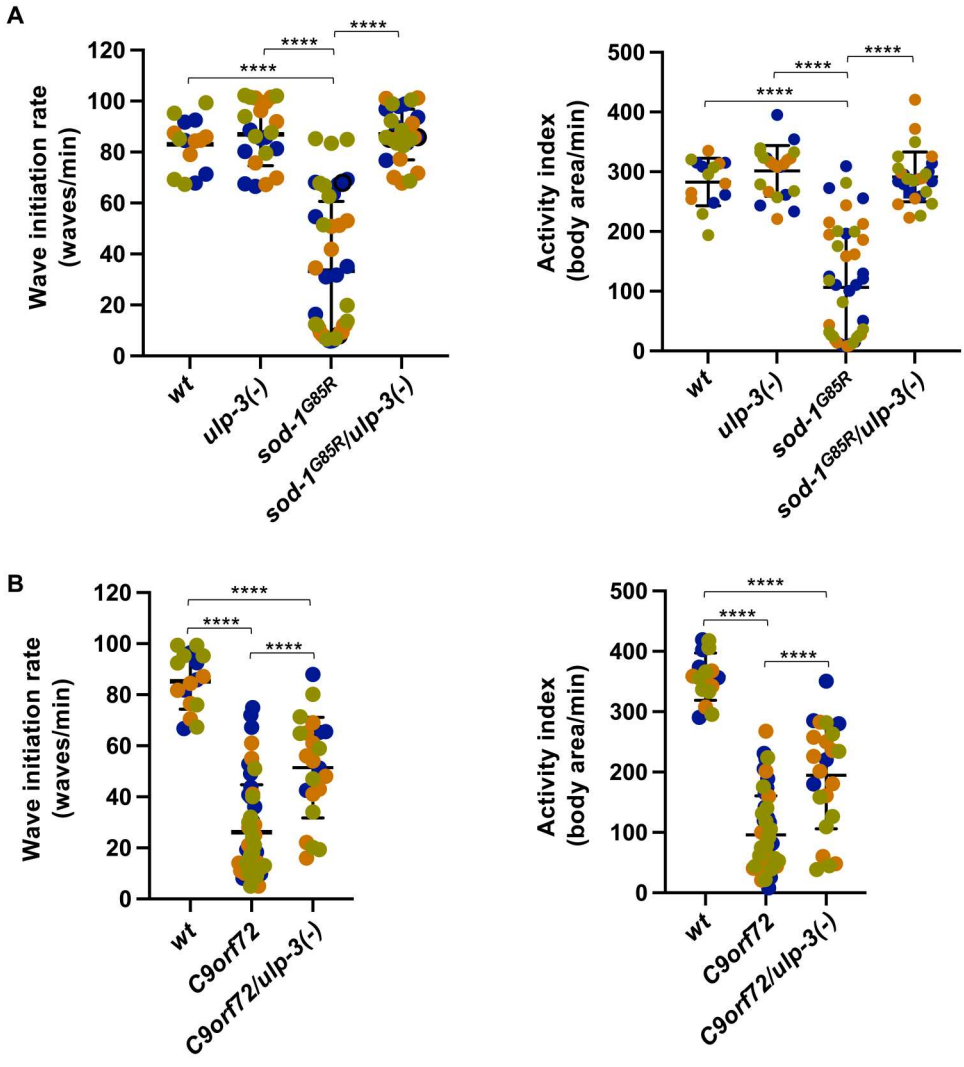

Fig. 8. Deletion of *ulp-3* (*nedp1*) rescues ALS phenotypes related to motility in the *sod-1*^{G85R} *and C9orf72 C. elegans* ALS model systems. Motility experiments were performed as described in Materials and Methods using two different parameters, wave initiation rate (left) and activity index (right) in the *sod-1*^{G85R} (**A**) and *C9orf72* (**B**) background. Each dot represents the values from one animal (5 to 18 animals analyzed per condition per experiment), and each color represents an independent experiment (n = 3).

NEDD8 may also control SG dynamics, our analysis defined PARP-1 as a key NEDD8 substrate through which NEDP1 controls SG dynamics, particularly the disassembly process. The use of PARP-1 mutants deficient for NEDDylation revealed that covalent NEDD8 modification of PARP-1 reduces PARylation. We cannot, however, exclude that the previously reported noncovalent interaction of PARP-1 with NEDD8 (*46*) contributes to PARP-1 activity control upon oxidative stress. In addition, NEDD8 may reduce PARP-1 activity through competition for lysine modifications with other members of the family, such as SUMO-2 and/or ubiquitin that are reported to promote PARP-1–dependent PARylation (*69*, *70*). Similar competition mechanisms of activity control by NEDDylation have been reported for other NEDD8 substrates, including ribosomal proteins (*32*).

The analysis on SG morphology and dynamics suggests that the reduced PARP-1 activity observed upon NEDP1 inhibition is the mechanism for the generation of smaller SGs. As discussed above, this could be the basis for the accelerated disassembly of SGs observed during recovery upon NEDP1 inhibition. This proposed mechanism is supported from the observation that a common phenotypic characteristic between chemical/genetic inactivation of PARP-1 and NEDP1 inhibition is the generation of smaller SGs that are eliminated faster during recovery compared to control cells. The use of PARP-1 mutants deficient for NEDDylation further supports this notion as their expression produces higher levels of PAR and generates larger and persistent SGs compared to wild-type PARP-1. In addition, the lack of an additive/synergistic effect of PARP-1 inhibitors on SG size/number/disassembly in NEDP1 KO cells strongly indicates the functional link between NEDP1 and PARP-1 for SG regulation.

Several lines of evidence have established that the PARP-1 product, PAR, either by directly modifying substrates or through formation of unanchored chains, creates the scaffold that allows the formation and growth of SGs (*49*, *71*). Whether PAR equally

affects the different steps in SG formation (core/shell formation and fusion) is still unclear. What is, however, emerging is that PAR production has to be modulated, especially for SG disassembly. Excessive production of PAR, due to PARP overactivation and/or inhibition of PAR glycohydrolases, delays SG disassembly during recovery and results in the formation of aberrant inclusions especially for disease-related mutant SG proteins (*48*, *49*, *71*). It is possible that the observed changes in SG mobility upon NEDP1 inhibition are related to the reduced levels of PAR produced during stress. NEDP1 may control SG mobility and growth by modulating stress-induced PARP-1 hyperactivation.

On the basis of the above-described role of PARP-1 in SG dynamics, PARP-1 inhibitors have been proposed as an attractive therapeutic approach for the elimination of aberrant SGs (*49*, *71*). However, this approach has several drawbacks since PARP-1 inhibitors also induce DNA damage and cell toxicity, effects that are desired for cancer treatment, but not for the treatment of neurodegenerative diseases. A proposed concept to overcome this problem is the development of low-toxicity PARP-1 inhibitors that will not affect the DNA damage response but will still retain their ability to prevent PARP-1 hyperactivation and promote aberrant inclusion elimination (*48*, *49*, *71*). NEDP1 KO/inhibition in several organisms including *C. elegans, Drosophila*, *Arabidopsis*, and *Schizosaccharomyces pombe* has no effect on survival/development but rather plays an important role in the cellular stress responses (*32*). In particular, genetic studies showed that NEDP1 inhibition blocks DNA damage–induced apoptosis and improves cell survival, with no effect in the DNA damage checkpoint signaling pathway (*45*). Thus, targeting NEDP1 may provide the desired modulation of PARP-1: to reduce PARP-1 hyperactivation and to promote the disassembly of pathogenic SGs, in the absence of any toxic effects. The study reveals NEDP1 as a potential target to ameliorate ALS-related phenotypes and provides the proof of principle for the use of anti-NEDP1 Nbs as attractive therapeutic agents for ALS. Antibodies/Nbs have received wide attention as tools to directly target and eliminate misfolded proteins or aberrant inclusions for the development of immunotherapeutics in proteinopathies (*72*). The presented NEDP1 Nb highlights that targeting instead processes that regulate the dynamics and elimination of aberrant SGs is an attractive alternative therapeutic approach.

MATERIALS AND METHODS

Materials

The following antibodies were used: rabbit monoclonal anti-NEDD8, Y297 (#GTX61205, Abcam), rabbit anti-H2A (#Ab13923, Abcam), rabbit anti-ubiquitin (#z0458, DAKO), mouse anti–PARP-1 (F-2) (#sc-8007, Santa Cruz Biotechnology), mouse anti-TIA1 (G-3) (#sc-166247, Santa Cruz Biotechnology), mouse anti-eIF4G (A-10) (#sc-133155, Santa Cruz Biotechnology), mouse anti-PAR (10HA) (#4335-MC-100, Trevigen), mouse anti-GFP (#11814460001, Roche), mouse anti–β-tubulin (#3873, Cell Signaling Technology), sheep anti-NEDP1 (in house) (*51*), mouse anti-Flag (#A2220, Sigma-Aldrich), mouse anti-p53 (DO-1) (#sc-126, Santa Cruz Biotechnology), ubiquitin branch motif antibody (K-ε-GG), (#3925, Cell Signaling Technology), and secondary antibodies (anti-mouse #4416, anti-rabbit #A0545, and anti-sheep #A3415, Sigma-Aldrich). MLN4924 (NAEi) was purchased from Active Biochem (#A-1139); MLN7243 (UAEi) was purchased from Chemietek (#CT-M7243); and Fugene6 HD (#E2691, Promega), Lipofectamine 2000 (#11668019, Invitrogen), Ni–-nitrilotriacetic acid agarose (#30210, QIAGEN), polyvinylidene difluoride membrane (#LC2002, Millipore), ECL Western Blotting Detection Reagents (#RPN2232, Amersham), CellTiter-Glo Luminescent Cell Viability Assay (#G7570, Promega), MMS (#129925), CPT (#C9911), and etoposide (#E1383) were purchased from Sigma-Aldrich.

Worm strain and culture conditions

Hermaphrodite worms were maintained at 20°C on nematode growth medium (NGM) agar plates seeded with *E. coli* strain OP50. NGM plates contain 1.5% agar, 0.25% tryptone, 0.3% sodium chloride, 1 mM calcium chloride, 1 mM magnesium sulfate, 25 mM potassium phosphate (pH 6.0), and cholesterol (5 μg/ml). Double and triple mutants were isolated by polymerase chain reaction and confirmed by genomic sequencing. Mutants generated in this study will be deposited at the Caenorhabditis Genetics Center (CGC) and/or will be provided on request.

The following strains were used in the study: *wt:* N2 (Bristol); *ulp-3(tm1287) IV* (DPX1287); *sod-1(rt449[G85RC]) II* (HA2987); *gtbp-1(ax2055[gtbp-1::GFP]) IV* (JH3199); *ulp-3(tm1287) IV, gtbp-1(ax2055[gtbp-1::GFP]) IV* (DPX11); *sod-1(rt449[G85RC]) II; gtbp-1(ax2055[gtbp-1::GFP]) IV* (DPX12); *sod-1(rt449[G85RC]) II; gtbp-1(ax2055[gtbp-1::GFP]) IV, ulp-3(tm1287) IV* (DPX13); *csIs(pqn-59::GFP) I; gtbp-1::RFP(ax5000) IV* (HML713); *kasls7[snb-1p::C9 ubi + myo-2::GFP]* (KRA315); *kasls7[snb-1p::C9 ubi + myo-2::GFP]; ulp-3(tm1287) IV* (DXP20); *kasls7[snb-1p::C9 ubi + myo-2::GFP]; gtbp-1::RFP(ax5000) IV* (DPX21); *kasls7[snb-1p::C9 ubi + myo-2::GFP]; gtbp-1::RFP(ax5000), ulp-3(tm1287)* IV (DPX22); *gtbp-1::RFP(ax5000) IV* (DPX23); and *gtbp-1::RFP(ax5000), ulp-3(tm1287) IV* (DPX24).

Fibroblasts

The following set of human-derived fibroblasts were used: HDF20 Female 63 years old, fibroblast passage 9; 37/15 sALS Female 59 years old, fibroblast passage 6.

Cell culture

Cell lines, U2OS (female) preferred system for live imaging, HCT116 (female) preferred system for diGly proteomics based on previous studies (*55*), and HEK293 (male), preferred system for transient overexpression studies due to high transfection efficiency, were originally obtained from the American Type Culture Collection bioresource. Cell lines were maintained in Dulbecco's modified Eagle's medium (DMEM), 10% fetal calf serum (FCS), and standard antibiotics (streptomycin and penicillin), 5% CO_2 and 37°C, and regularly tested for mycoplasma contamination. Cell lines have not been authenticated. Stable cell lines expressing His6-NEDD8 were established using puromycin (2.5 μg/ml) as described in (*73*). For cell lines stably expressing GFP-G3BP1, cells were selected with G418 (1 mg/ml) for 14 days before a pool of cells stably expressing GFP-G3BP1 was acquired. U2OS NEDP1 KO cells were generated by CRISPR-Cas9 as previously described (*45*). Similar approaches were used to generate the HCT116 and HEK293 NEDP1 KO cells. The deletion within the *nedp1* gene was confirmed by DNA sequencing, and the absence of NEDP1 protein with concomitant accumulation of NEDD8 conjugates was confirmed by Western blot analysis. Parental and NEDP1 KO U2OS cells were

infected with EB1-mcherry–expressing vector virus (gift from B. Vitre). Cells were selected with puromycin (2.5 μg/ml). Dissected mouse-derived hippocampal neurons were plated in medium A (Neurobasal, B27, 10% FCS, GlutaMAX, 25 μM glutamic acid, streptomycin/penicillin) for 2 hours before changing into medium B (Neurobasal, B27, GlutaMAX, 0.45% glucose, and streptomycin/penicillin), whereas fibroblasts derived from ALS patients were grown in high-glucose DMEM (without sodium pyruvate), supplemented with 2 mM L-glutamine, penicillin/streptomycin (100 U/ml), and 10% fetal bovine serum.

Transfection

U2OS cells were transfected with the indicated plasmids with Fugene 6 (Roche) according to the manufacturer's instructions using a 3:1 Fugene/plasmid ratio. For HEK293, the calcium/phosphate method was used. Transfection of mouse-derived hippocampal neurons was performed using Lipofectamine 2000.

Retrovirus production

The Nb9-expressing DNA was cloned in the pMXs-Puro retroviral vector and cotransfected in 10-cm cell culture dishes of 5×10^6 HEK293T cells, with virus packaging and envelope-expressing plasmids using Fugene-6 (Roche). The medium was replaced with DMEM with 10% FCS the next day, and supernatant was harvested 3 days after transfection, filtered through a 0.45-μm pore-size filter (Sartorius, Minisart), and stored at −80°C.

Isolation of His_6-tagged proteins

Isolation of His_6-NEDDylated proteins and His_6-PARP-1 was performed under denaturing conditions as described in (*74*).

SG assembly and recovery

For assembly, cells grown on coverslips in a 12-well plate were treated with 0.2 or 0.5 mM sodium arsenite for the indicated time before washing three times with phosphate-buffered saline (PBS) followed by fixation with 3.7% paraformaldehyde. For recovery, the medium containing arsenite was removed and the cells were washed three times with PBS and then incubated in fresh medium for the indicated time before fixation. Under the used arsenite treatment (1 hour, 0.5 mM), almost 100% of cells form SGs in all conditions and this was the point of recovery. Formation and recovery of SGs was evaluated by subsequent immunofluorescence analysis. Images of random fields were selected on each coverslip to quantify the percentage of cells with SGs in each condition. The size and the number of SGs were manually measured with ImageJ. The same batch of arsenite was used for each experiment and its independent replicates to avoid variations in the timing of the SG response due to arsenite batch differences. In the experiments where NAEi and UAEi were used, the equivalent volume of dimethyl sulfoxide (solvent used to dissolve the compounds) was added in the untreated/control conditions. For hippocampal neurons, cells were seeded in six-well plates on coverslips coated with poly-L-ornithine (0.25 mg/ml). Thirty minutes before transfection, fresh medium with no glucose was added and cells were transfected with TIA1 (1 μg) and Nb9 (2 μg) expression plasmids using Lipofectamine 2000 (6 μl). Forty-eight hours after transfection, cells were stressed with arsenite (0.2 mM) for 1 hour before medium was replaced for the recovery period (2.5 hours). Cells were fixed with 4% paraformaldehyde for 10 min before analysis for GFP fluorescence. For the fibroblasts derived from ALS patients, cells at a density of 3×10^5 cells/ml were seeded on 12-cm^2 coverslips coated with collagen. Control or Nb9-expressing retrovirus was applied onto the medium, and cells were centrifuged at 3500 rpm for 90 min at 37°C. Forty-eight hours after infection, cells were treated with 0.5 mM arsenite and allowed to recover in fresh medium before immunostaining.

Immunofluorescence staining

Cells were plated on coverslips in a 12-well plate and, the day after, were transfected as indicated. Cells were washed with PBS, fixed with 3.7% paraformaldehyde in PBS for 15 min, and then permeabilized with 1% Triton X-100 in PBS at room temperature (RT) for 10 min. Cells were blocked with 1% goat serum in 0.05% PBS–Tween for 30 min and then incubated with primary antibody (diluted in 1% goat serum in 0.05% PBS–Tween) for 16 hours. After washes in 0.05% PBS–Tween, coverslips were incubated with fluorescein isothiocyanate (FITC)– or tetramethyl rhodamine isothiocyanate (TRITC)–conjugated donkey anti-mouse or donkey anti-rabbit secondary antibodies (diluted in 1% goat serum in 0.05% PBS–Tween) at RT for 1 hour. DNA was stained with 4′,6-diamidino-2-phenylindole (1:20,000) at RT for 1 min. After mounting with ProLong Gold Antifade reagent (Molecular Probes), images were acquired with a Zeiss Axio Imager Z2 microscope with a 40× Plan Neofluar 1.3 NA (oil) or a 63× Plan Apochromat 1.4 NA oil objective and a scMOS ZYLA 5.5 camera controlled by the MetaMorph software (Universal Imaging, Roper Scientific). Images were treated with ImageJ or Fiji.

Live-cell microscopy

For live-cell microscopy, images were acquired using a 40× LUCPLFLN 0.6NA RC2 lens on an Inverted Olympus IX83 microscope controlled by MetaMorph software and equipped with a full-enclosure environmental chamber heated to 37°C with 5% CO_2 and a 1 ZYLA 4.2 MP scMOS camera. Frames were recorded every 3 min over 1 hour for SG assembly and every 30 min for 16 hours for SG recovery. Parental and NEDP1 KO U2OS cells were followed during the same time lapse. Images were imported as a sequence and analyzed using the Fiji software. Fiji was also used for brightness adjustment, cropping, and creating scale bars and insets.

Fluorescence recovery after photobleaching

Parental or NEDP1 KO U2OS cells were grown on μ-Slide 8 Well—ibiTreat (ibidi GmbH, Gräfelfing, Germany). Immediately before imaging, cells were treated with 0.2 mM arsenite and placed on a heated chamber at 37°C with 5% CO_2. Imaging and photobleaching were performed with an apochromat ×100 oil objective using a Nikon TIRF PALM STORM inverted microscope. A 488-nm laser was used to photobleach G3BP1 inclusion after 1 and 2 hours of arsenite treatment. Immediately after bleaching, the images were collected every 50 ms for a total of 300 frames as a post-bleached sample. The fluorescence intensities of post-bleached G3BP1 inclusions (BL) were individually measured. In the meantime, the fluorescence intensities of nonbleached G3BP1 inclusions were measured as a reference control (REF). Also, the fluorescence intensities of background were measured as a background control (BG). To obtain corrected values (corr1), (BG) values were subtracted from Bleach (BL) and Reference (REF): $BL\_corr1(t) = BL(t) - BG(t)$; $REF\_corr1(t) = REF(t) - BG(t)$, and then the corrected

Bleach values were normalized to corrected Reference values: $BL\_corr2(t) = BL\_corr1(t)/REF\_corr1(t)$. The mean prebleach intensity was used to normalize the corrected bleach value: $BL\_corr3(t) = BL\_corr2(t)/BL\_corr2$(prebleach). The mean prebleach value represents the maximum intensity to which the bleached region could possibly recover. The percentage of mobile fraction and the half time of recovery were obtained by using the curve fitting function/exponential recovery in Fiji.

Microtubule dynamics

For the time-lapse acquisition of EB1-mcherry signal, parental and NEDP1 KO U2OS cells stably expressing EB1-mcherry were imaged with a Nikon inverted microscope coupled to the Andor Dragonfly spinning disk. Images were acquired using an EMCCD iXon888 Life Andor camera (pixel size: 0.11 μm) with a 100× oil-immersion objective (Plan Apo lambda 1.45 NA 0.13 mm WD). Images were acquired every 0.3 s during 45 s at 37°C in a thermo-regulated atmosphere. Signal was then tracked in each individual cell using Matlab and the PlusTipTracker (*75*) open source software package with the following parameters: σ1 = 1, σ2 = 4, $K = 3$, search radius range = 1 to 5 pixels, minimum subtrack length = three frames, maximum gap length = 30 frames, maximum shrinkage factor = 1.5, maximum angle forward = 30°, maximum angle backward = 10°, and fluctuation radius = 2 pixels. Results tables were then exported and further analyzed using Excel.

Fluorescence-activated cell sorting analysis

U2OS cells (6-cm dishes) were transfected with either empty or GFP-expressing pcDNA3 construct (1 μg). Forty-eight hours after transfection, cells were harvested and processed on Aria IIU Becton Dickinson cytometer, and data were analyzed by FACSDiVa software.

Cell viability–clonogenic assays

For cell viability assays, cells were seeded in 96-well plates (500 cells per well) and treated as indicated. Cell viability was measured in triplicates using the CellTiter-Glo Luminescence assays from Promega or by counting live cells using Countess 3 (Invitrogen) according to the manufacturer′s instructions. For the clonogenic assay, cells were seeded in six-well plates (20,000 cells per well) and treated as indicated. Plates were washed, fixed with methanol for 20 min at RT, and dried, and colonies were stained with Giemsa stain and counted.

Western blot analysis

Extracts were prepared by lysing cells in 2× SDS Laemmli buffer. Proteins were mainly resolved on precast Novex (Invitrogen) 4 to 12% gradient SDS polyacrylamide gels and transferred onto nitrocellulose membrane (GE Healthcare). Membranes were washed once with PBS and blocked with 5% milk solution (PBS, 0.1% Tween 20, and 5% skimmed milk) for 1 hour at RT with gentle agitation. Then, membranes were washed three times with PBST (PBS with 0.1% Tween 20) for 10 min each and incubated with primary antibodies (diluted in PBS, 0.1% Tween 20, 3% bovine serum albumin, and 0.1% NaN_3) overnight at 4°C or for 3 hours at RT with gentle agitation. After washing three times with PBST for 15 min, membranes were incubated with secondary antibodies diluted in 5% milk solution for 1 hour at RT with gentle agitation. Then, membranes were washed three times with PBST and two times with PBS for 15 min each before they were soaked in ECL Western Blot Detection solution (Amersham) and exposed to Medical Films (Konica Minolta).

Mass spectrometry

Diglycine motif peptide identification was performed by Cell Signaling Technology, following UbiScan protocols and instructions (Cell Signaling Technology) using ubiquitin branch motif antibody (K-ε-GG) #3925. Peptides were loaded onto 10 cm × 75 μm PicoFrit Capillary column packed with Magic C18 AQ reversed-phase resin. The column was developed with a 90-min linear gradient of acetonitrile in 0.125% formic acid delivered at 280 nl/min. MS parameters settings are as follows: MS run time, 96 min; MS1 scan range, 300.0 to 1500.00, and top 20 MS/MS [min signal, 500; isolation width, 2.0; normalized coll. energy, 35.0; activation-Q, 0.250; activation time, 20.0; lock mass, 371.101237; charge state rejection enabled; charge state, 1+ rejected; dynamic exclusion enabled; repeat count, 1; repeat duration, 35.0; exclusion list size, 500; exclusion duration, 40.0; exclusion mass width relative to mass; exclusion mass width, 10 parts per million (ppm)]. MS/MS spectra were evaluated using SEQUEST 3G and the SORCERER 2 platform from Sage-N Research (v4.0, Milpitas, CA). Searches were performed against the most recent update of the National Center for Biotechnology Information (NCBI) human database with mass accuracy of ±50 ppm for precursor ions and 1 Da for product ions. Results were filtered with mass accuracy of ±5 ppm on precursor ions and the presence of the intended motif (K-ε-GG). LTQ-Orbitrap Velos was used (Thermo Fisher Scientific). A 5% default false-positive rate was used to filter the SORCERER results.

PARP-1 site-directed mutagenesis

All KR PARP-1 mutants were generated by site-directed mutagenesis, and sequences were verified by automated sequencing.

Imaging of *C. elegans*

For imaging of SGs, GFP–GTBP-1–expressing young adults (L4) were placed on a fresh NGM-seeded plate, and for heat shock, plates were incubated at 30°C for 4 hours.

For the arsenite treatment, unseeded NGM plates were soaked with sodium arsenite to achieve a final concentration of 10 mM. Arsenite-coated plates were then seeded with bacteria, and young adults were placed on these plates for 2 hours. After treatment, animals were mounted on 2% (w/v) agarose pads and immobilized using 25 mM levamisole in M9 buffer. Images of the anterior region of the worm consisting of pharynx were captured using a fluorescence microscope (Zeiss AxioImager Z2) with a Plan-Apochromat 100×/1.40 oil objective using ZEN software (version 3.4.91, Blue edition). Representative images are presented following max-project of Z-stacked images using maximum intensity projection type with Fiji ImageJ software (version 2.3.0/1.53f). SGs were counted using cell counter plugin. The size of SGs was measured using ImageJ.

Swimming behavior (motility) assay

The protocol described in (*65*) was used. Young adults (L4) were treated overnight with 5 mM paraquat (oxidative stress) in NGM-seeded plates. Three worms were placed in a drop of 5 μl of M9 buffer inside the ring drawn using a hydrophobic PAP pen on microscopic slide. Movies were recorded at 22 frames/s for 30 s and

analyzed with the CeleST software in Matlab R2019b (version 9.7.0.1216025; MathWorks Inc., Natick, MA, USA). Worms were randomly selected for analysis, and the number of body waves initiated from either the head or tail per minute is presented as wave initiation rate. Swimming rates from three repeats are presented.

Statistical analysis

Leica LAS (FRAP analysis), SEQUEST 3G and SORCERER 2 (mass spectrometry analysis), GraphPad Prism, PlusTipTracker, ImageJ, and Cytoscape were used. For SG assembly/disassembly process, about 100 cells randomly selected per condition were scored for the presence of SGs. Statistical significance was calculated by Mann-Whitney test; ns: nonsignificant; $*P < 0.05$; $**P < 0.01$; $***P < 0.001$; $****P < 0.0001$. In all experiments, n values represent the number of independent experiments, as indicated in figure legends.

Supplementary Materials

This PDF file includes:
Figs. S1 to S7
Legends for movies S1 to S11
Legends for data S1 and S2

Other Supplementary Material for this manuscript includes the following:
Movies S1 to S11
Data S1 and S2

REFERENCES AND NOTES

1. I. Amm, T. Sommer, D. H. Wolf, Protein quality control and elimination of protein waste: The role of the ubiquitin–proteasome system. *Biochim. Biophys. Acta Mol. Cell Res.* **1843**, 182–196 (2014).
2. H. Yoo, J. A. M. Bard, E. V. Pilipenko, D. A. Drummond, Chaperones directly and efficiently disperse stress-triggered biomolecular condensates. *Mol. Cell* **82**, 741–755.e11 (2022).
3. E. M. Sontag, R. S. Samant, J. Frydman, Mechanisms and functions of spatial protein quality control. *Annu. Rev. Biochem.* **86**, 97–122 (2017).
4. S. Alberti, A. A. Hyman, Biomolecular condensates at the nexus of cellular stress, protein aggregation disease and ageing. *Nat. Rev. Mol. Cell Biol.* **22**, 196–213 (2021).
5. M. G. Iadanza, M. P. Jackson, E. W. Hewitt, N. A. Ranson, S. E. Radford, A new era for understanding amyloid structures and disease. *Nat. Rev. Mol. Cell Biol.* **19**, 755–773 (2018).
6. C. Iserman, C. Desroches Altamirano, C. Jegers, U. Friedrich, T. Zarin, A. W. Fritsch, M. Mittasch, A. Domingues, L. Hersemann, M. Jahnel, D. Richter, U.-P. Guenther, M. W. Hentze, A. M. Moses, A. A. Hyman, G. Kramer, M. Kreysing, T. M. Franzmann, S. Alberti, Condensation of Ded1p promotes a translational switch from housekeeping to stress protein production. *Cell* **181**, 818–831.e19 (2020).
7. S. Wegmann, B. Eftekharzadeh, K. Tepper, K. M. Zoltowska, R. E. Bennett, S. Dujardin, P. R. Laskowski, D. MacKenzie, T. Kamath, C. Commins, C. Vanderburg, A. D. Roe, Z. Fan, A. M. Molliex, A. Hernandez-Vega, D. Muller, A. A. Hyman, E. Mandelkow, J. P. Taylor, B. T. Hyman, Tau protein liquid-liquid phase separation can initiate tau aggregation. *EMBO J.* **37**, e98049 (2018).
8. Y. Shen, F. S. Ruggeri, D. Vigolo, A. Kamada, S. Qamar, A. Levin, C. Iserman, S. Alberti, P. S. George-Hyslop, T. P. J. Knowles, Biomolecular condensates undergo a generic shear-mediated liquid-to-solid transition. *Nat. Nanotechnol.* **15**, 841–847 (2020).
9. N. Kedersha, P. Anderson, Stress granules: Sites of mRNA triage that regulate mRNA stability and translatability. *Biochem. Soc. Trans.* **30**, 963–969 (2002).
10. D. W. Sanders, N. Kedersha, D. S. W. Lee, A. R. Strom, V. Drake, J. A. Riback, D. Bracha, J. M. Eeftens, A. Iwanicki, A. Wang, M.-T. Wei, G. Whitney, S. M. Lyons, P. Anderson, W. M. Jacobs, P. Ivanov, C. P. Brangwynne, Competing protein-RNA interaction networks control multiphase intracellular organization. *Cell* **181**, 306–324.e28 (2020).
11. J. R. Wheeler, T. Matheny, S. Jain, R. Abrisch, R. Parker, Distinct stages in stress granule assembly and disassembly. *eLife* **5**, e18413 (2016).
12. J. P. Taylor, J. Hardy, K. H. Fischbeck, Toxic proteins in neurodegenerative disease. *Science* **296**, 1991–1995 (2002).
13. G. Kim, O. Gautier, E. Tassoni-Tsuchida, X. R. Ma, A. D. Gitler, ALS genetics: Gains, losses, and implications for future therapies. *Neuron* **108**, 822–842 (2020).
14. A. Patel, H. O. Lee, L. Jawerth, S. Maharana, M. Jahnel, M. Y. Hein, S. Stoynov, J. Mahamid, S. Saha, T. M. Franzmann, A. Pozniakovski, I. Poser, N. Maghelli, L. A. Royer, M. Weigert, E. W. Myers, S. Grill, D. Drechsel, A. A. Hyman, S. Alberti, A liquid-to-solid phase transition of the ALS protein FUS accelerated by disease mutation. *Cell* **162**, 1066–1077 (2015).
15. A. Molliex, J. Temirov, J. Lee, M. Coughlin, A. P. Kanagaraj, H. J. Kim, T. Mittag, J. P. Taylor, Phase separation by low complexity domains promotes stress granule assembly and drives pathological fibrillization. *Cell* **163**, 123–133 (2015).
16. D. Mateju, T. M. Franzmann, A. Patel, A. Kopach, E. E. Boczek, S. Maharana, H. O. Lee, S. Carra, A. A. Hyman, S. Alberti, An aberrant phase transition of stress granules triggered by misfolded protein and prevented by chaperone function. *EMBO J.* **36**, 1669–1687 (2017).
17. P. Zhang, B. Fan, P. Yang, J. Temirov, J. Messing, H. J. Kim, J. P. Taylor, Chronic optogenetic induction of stress granules is cytotoxic and reveals the evolution of ALS-FTD pathology. *eLife* **8**, e39578 (2019).
18. I. R. Mackenzie, A. M. Nicholson, M. Sarkar, J. Messing, M. D. Purice, C. Pottier, K. Annu, M. Baker, R. B. Perkerson, A. Kurti, B. J. Matchett, T. Mittag, J. Temirov, G.-Y. R. Hsiung, C. Krieger, M. E. Murray, M. Kato, J. D. Fryer, L. Petrucelli, L. Zinman, S. Weintraub, M. Mesulam, J. Keith, S. A. Zivkovic, V. Hirsch-Reinshagen, R. P. Roos, S. Züchner, N. R. Graff-Radford, R. C. Petersen, R. J. Caselli, Z. K. Wszolek, E. Finger, C. Lippa, D. Lacomis, H. Stewart, D. W. Dickson, H. J. Kim, E. Rogaeva, E. Bigio, K. B. Boylan, J. P. Taylor, R. Rademakers, TIA1 mutations in amyotrophic lateral sclerosis and frontotemporal dementia promote phase separation and alter stress granule dynamics. *Neuron* **95**, 808–816.e9 (2017).
19. M. Ganassi, D. Mateju, I. Bigi, L. Mediani, I. Poser, H. O. Lee, S. J. Seguin, F. F. Morelli, J. Vinet, G. Leo, O. Pansarasa, C. Cereda, A. Poletti, S. Alberti, S. Carra, A surveillance function of the HSPB8-BAG3-HSP70 chaperone complex ensures stress granule integrity and dynamism. *Mol. Cell* **63**, 796–810 (2016).
20. A. Turakhiya, S. R. Meyer, G. Marincola, S. Böhm, J. T. Vanselow, A. Schlosser, K. Hofmann, A. Buchberger, ZFAND1 recruits p97 and the 26S proteasome to promote the clearance of arsenite-induced stress granules. *Mol. Cell* **70**, 906–919.e7 (2018).
21. L. McGurk, E. Gomes, L. Guo, J. Mojsilovic-Petrovic, V. Tran, R. G. Kalb, J. Shorter, N. M. Bonini, Poly(ADP-ribose) prevents pathological phase separation of TDP-43 by promoting liquid demixing and stress granule localization. *Mol. Cell* **71**, 703–717.e9 (2018).
22. L. Streit, T. Kuhn, T. Vomhof, V. Bopp, A. C. Ludolph, J. H. Weishaupt, J. C. M. Gebhardt, J. Michaelis, K. M. Danzer, Stress induced TDP-43 mobility loss independent of stress granules. *Nat. Commun.* **13**, 5480 (2022).
23. F. Gasset-Rosa, S. Lu, H. Yu, C. Chen, Z. Melamed, L. Guo, J. Shorter, S. Da Cruz, D. W. Cleveland, Cytoplasmic TDP-43 de-mixing independent of stress granules drives inhibition of nuclear import, loss of nuclear TDP-43, and cell death. *Neuron* **102**, 339–357.e7 (2019).
24. J. R. Mann, A. M. Gleixner, J. C. Mauna, E. Gomes, M. R. DeChellis-Marks, P. G. Needham, K. E. Copley, B. Hurtle, B. Portz, N. J. Pyles, L. Guo, C. B. Calder, Z. P. Wills, U. B. Pandey, J. K. Kofler, J. L. Brodsky, A. Thathiah, J. Shorter, C. J. Donnelly, RNA binding antagonizes neurotoxic phase transitions of TDP-43. *Neuron* **102**, 321–338.e8 (2019).
25. J. Jiang, Q. Zhu, T. F. Gendron, S. Saberi, M. McAlonis-Downes, A. Seelman, J. E. Stauffer, P. Jafar-Nejad, K. Drenner, D. Schulte, S. Chun, S. Sun, S.-C. Ling, B. Myers, J. Engelhardt, M. Katz, M. Baughn, O. Platoshyn, M. Marsala, A. Watt, C. J. Heyser, M. C. Ard, L. De Muynck, L. M. Daughrity, D. A. Swing, L. Tessarollo, C. J. Jung, A. Delpoux, D. T. Utzschneider, S. M. Hedrick, P. J. de Jong, D. Edbauer, P. Van Damme, L. Petrucelli, C. E. Shaw, C. F. Bennett, S. Da Cruz, J. Ravits, F. Rigo, D. W. Cleveland, C. Lagier-Tourenne, Gain of toxicity from ALS/FTD-linked repeat expansions in *C9ORF72* is alleviated by antisense oligonucleotides targeting GGGGCC-containing RNAs. *Neuron* **90**, 535–550 (2016).
26. C. Lagier-Tourenne, M. Baughn, F. Rigo, S. Sun, P. Liu, H.-R. Li, J. Jiang, A. T. Watt, S. Chun, M. Katz, J. Qiu, Y. Sun, S.-C. Ling, Q. Zhu, M. Polymenidou, K. Drenner, J. W. Artates, M. McAlonis-Downes, S. Markmiller, K. R. Hutt, D. P. Pizzo, J. Cady, M. B. Harms, R. H. Baloh, S. R. Vandenberg, G. W. Yeo, X.-D. Fu, C. F. Bennett, D. W. Cleveland, J. Ravits, Targeted degradation of sense and antisense *C9orf72* RNA foci as therapy for ALS and frontotemporal degeneration. *Proc. Natl. Acad. Sci. U.S.A.* **110**, E4530–E4539 (2013).
27. A. McCampbell, T. Cole, A. J. Wegener, G. S. Tomassy, A. Setnicka, B. J. Farley, K. M. Schoch, M. L. Hoye, M. Shabsovich, L. Sun, Y. Luo, M. Zhang, N. Comfort, B. Wang, J. Amacker, S. Thankamony, D. W. Salzman, M. Cudkowicz, D. L. Graham, C. F. Bennett, H. B. Kordasiewicz, E. E. Swayze, T. M. Miller, Antisense oligonucleotides extend survival and reverse decrement in muscle response in ALS models. *J. Clin. Invest.* **128**, 3558–3567 (2018).
28. R. Malik, M. Wiedau, Therapeutic approaches targeting protein aggregation in amyotrophic lateral sclerosis. *Front. Mol. Neurosci.* **13**, 98 (2020).
29. N. Abidi, D. P. Xirodimas, Regulation of cancer-related pathways by protein NEDDylation and strategies for the use of NEDD8 inhibitors in the clinic. *Endocr. Relat. Cancer* **22**, T55–T70 (2015).

30. F. Liebelt, A. C. O. Vertegaal, Ubiquitin-dependent and independent roles of SUMO in proteostasis. *Am. J. Physiol. Cell Physiol.* **311**, C284–C296 (2016).
31. A. Williamson, A. Werner, M. Rape, The colossus of ubiquitylation: Decrypting a cellular code. *Mol. Cell* **49**, 591–600 (2013).
32. I. Meszka, J. Polanowska, D. P. Xirodimas, Mixed in chains: NEDD8 polymers in the Protein Quality Control system. *Semin. Cell Dev. Biol.* **132**, 27–37 (2022).
33. C. L. Bennett, A. R. La Spada, SUMOylated Senataxin functions in genome stability, RNA degradation, and stress granule disassembly, and is linked with inherited ataxia and motor neuron disease. *Mol. Genet. Genomic Med.* **9**, e1745 (2021).
34. Y. Gwon, B. A. Maxwell, R.-M. Kolaitis, P. Zhang, H. J. Kim, J. P. Taylor, Ubiquitination of G3BP1 mediates stress granule disassembly in a context-specific manner. *Science* **372**, eabf6548 (2021).
35. J. Jongjitwimol, R. A. Baldock, S. J. Morley, F. Z. Watts, Sumoylation of eIF4A2 affects stress granule formation. *J. Cell Sci.* **129**, 2407–2415 (2016).
36. J. Keiten-Schmitz, K. Wagner, T. Piller, M. Kaulich, S. Alberti, S. Müller, The nuclear SUMO-targeted ubiquitin quality control network regulates the dynamics of cytoplasmic stress granules. *Mol Cell* **79**, 54–67.e7 (2020).
37. H. Marmor-Kollet, A. Siany, N. Kedersha, N. Knafo, N. Rivkin, Y. M. Danino, T. G. Moens, T. Olender, D. Sheban, N. Cohen, T. Dadosh, Y. Addadi, R. Ravid, C. Eitan, B. Toth Cohen, S. Hofmann, C. L. Riggs, V. M. Advani, A. Higginbottom, J. Cooper-Knock, J. H. Hanna, Y. Merbl, L. Van Den Bosch, P. Anderson, P. Ivanov, T. Geiger, E. Hornstein, Spatiotemporal proteomic analysis of stress granule disassembly using APEX reveals regulation by SUMOylation and links to ALS pathogenesis. *Mol. Cell* **80**, 876–891.e6 (2020).
38. B. A. Maxwell, Y. Gwon, A. Mishra, J. Peng, H. Nakamura, K. Zhang, H. J. Kim, J. P. Taylor, Ubiquitination is essential for recovery of cellular activities after heat shock. *Science* **372**, eabc3593 (2021).
39. N. Tolay, A. Buchberger, Comparative profiling of stress granule clearance reveals differential contributions of the ubiquitin system. *Life Sci. Alliance* **4**, e202000927 (2021).
40. A. K. Jayabalan, A. Sanchez, R. Y. Park, S. P. Yoon, G.-Y. Kang, J.-H. Baek, P. Anderson, Y. Kee, T. Ohn, NEDDylation promotes stress granule assembly. *Nat. Commun.* **7**, 12125 (2016).
41. S. Markmiller, A. Fulzele, R. Higgins, M. Leonard, G. W. Yeo, E. J. Bennett, Active protein neddylation or ubiquitylation is dispensable for stress granule dynamics. *Cell Rep.* **27**, 1356–1363.e3 (2019).
42. S. M. Lange, L. A. Armstrong, Y. Kulathu, Deubiquitinases: From mechanisms to their inhibition by small molecules. *Mol. Cell* **82**, 15–29 (2022).
43. R. I. Enchev, B. A. Schulman, M. Peter, Protein neddylation: Beyond cullin–RING ligases. *Nat. Rev. Mol. Cell Biol.* **16**, 30–44 (2014).
44. E. Santonico, Old and new concepts in ubiquitin and NEDD8 recognition. *Biomolecules* **10**, 566 (2020).
45. A. P. Bailly, A. Perrin, M. Serrano-Macia, C. Maghames, O. Leidecker, H. Trauchessec, M. L. Martinez-Chantar, A. Gartner, D. P. Xirodimas, The balance between mono- and NEDD8-chains controlled by NEDP1 upon DNA damage is a regulatory module of the HSP70 ATPase activity. *Cell Rep.* **29**, 212–224.e8 (2019).
46. M. J. Keuss, R. Hjerpe, O. Hsia, R. Gourlay, R. Burchmore, M. Trost, T. Kurz, Unanchored tri-NEDD8 inhibits PARP-1 to protect from oxidative stress-induced cell death. *EMBO J.* **38**, e100024 (2019).
47. K. Vijayasimha, B. P. Dolan, The many potential fates of non-canonical protein substrates subject to NEDDylation. *Cell* **10**, 2660 (2021).
48. Y. Duan, A. Du, J. Gu, G. Duan, C. Wang, X. Gui, Z. Ma, B. Qian, X. Deng, K. Zhang, L. Sun, K. Tian, Y. Zhang, H. Jiang, C. Liu, Y. Fang, PARylation regulates stress granule dynamics, phase separation, and neurotoxicity of disease-related RNA-binding proteins. *Cell Res.* **29**, 233–247 (2019).
49. X. Jin, X. Cao, S. Liu, B. Liu, Functional roles of poly(ADP-ribose) in stress granule formation and dynamics. *Front. Cell Dev. Biol.* **9**, 671780 (2021).
50. H. Tourrière, K. Chebli, L. Zekri, B. Courselaud, J. M. Blanchard, E. Bertrand, J. Tazi, The RasGAP-associated endoribonuclease G3BP assembles stress granules. *J. Cell Biol.* **160**, 823–831 (2003).
51. L. Shen, H. Liu, C. Dong, D. Xirodimas, J. H. Naismith, R. T. Hay, Structural basis of NEDD8 ubiquitin discrimination by the deNEDDylating enzyme NEDP1. *EMBO J.* **24**, 1341–1351 (2005).
52. O. Leidecker, I. Matic, B. Mahata, E. Pion, D. P. Xirodimas, The ubiquitin E1 enzyme Ube1 mediates NEDD8 activation under diverse stress conditions. *Cell Cycle* **11**, 1142–1150 (2012).
53. N. Abidi, H. Trauchessec, G. Hassanzadeh-Ghassabeh, M. Pugniere, S. Muyldermans, D. P. Xirodimas, Development of nanobodies as first-in-class inhibitors for the NEDP1 deNEDDylating enzyme. bioRxiv 999326 [Preprint] (23 March 2020). https://doi.org/10.1101/2020.03.20.999326.
54. E. S. Nadezhdina, A. J. Lomakin, A. A. Shpilman, E. M. Chudinova, P. A. Ivanov, Microtubules govern stress granule mobility and dynamics. *Biochim. Biophys. Acta Mol. Cell Res.* **1803**, 361–371 (2010).
55. S. Lobato-Gil, J. B. Heidelberger, C. M. Maghames, A. Bailly, L. Brunello, M. S. Rodriguez, P. Beli, D. P. Xirodimas, Proteome-wide identification of NEDD8 modification sites reveals distinct proteomes for canonical and atypical NEDDylation. *Cell Rep.* **34**, 108635 (2020).
56. A. M. Vogl, L. Phu, R. Becerra, S. A. Giusti, E. Verschueren, T. B. Hinkle, M. D. Bordenave, M. Adrian, A. Heidersbach, P. Yankilevich, F. D. Stefani, W. Wurst, C. C. Hoogenraad, D. S. Kirkpatrick, D. Refojo, M. Sheng, Global site-specific neddylation profiling reveals that NEDDylated cofilin regulates actin dynamics. *Nat. Struct. Mol. Biol.* **27**, 210–220 (2020).
57. H. Hanzlikova, W. Gittens, K. Krejcikova, Z. Zeng, K. W. Caldecott, Overlapping roles for PARP1 and PARP2 in the recruitment of endogenous XRCC1 and PNKP into oxidized chromatin. *Nucleic Acids Res.* **45**, gkw1246 (2016).
58. S. N. Baskoylu, J. Yersak, P. O'Hern, S. Grosser, J. Simon, S. Kim, K. Schuch, M. Dimitriadi, K. S. Yanagi, J. Lins, A. C. Hart, Single copy/knock-in models of ALS SOD1 in *C. elegans* suggest loss and gain of function have different contributions to cholinergic and glutamatergic neurodegeneration. *PLOS Genet.* **14**, e1007682 (2018).
59. K. Forsberg, P. A. Jonsson, P. M. Andersen, D. Bergemalm, K. S. Graffmo, M. Hultdin, J. Jacobsson, R. Rosquist, S. L. Marklund, T. Brännström, Novel antibodies reveal inclusions containing non-native SOD1 in sporadic ALS patients. *PLOS ONE* **5**, e11552 (2010).
60. C. Carlston, R. Weinmann, N. Stec, S. Abbatemarco, F. Schwager, J. Wang, H. Ouyang, C. Y. Ewald, M. Gotta, C. M. Hammell, PQN-59 antagonizes microRNA-mediated repression during post-embryonic temporal patterning and modulates translation and stress granule formation in *C. elegans*. *PLOS Genet.* **17**, e1009599 (2021).
61. Y. Sonobe, J. Aburas, G. Krishnan, A. C. Fleming, G. Ghadge, P. Islam, E. C. Warren, Y. Gu, M. W. Kankel, A. E. X. Brown, E. Kiskinis, T. F. Gendron, F.-B. Gao, R. P. Roos, P. Kratsios, A *C. elegans* model of *C9orf72*-associated ALS/FTD uncovers a conserved role for eIF2D in RAN translation. *Nat. Commun.* **12**, 6025 (2021).
62. A. E. Renton, E. Majounie, A. Waite, J. Simón-Sánchez, S. Rollinson, J. R. Gibbs, J. C. Schymick, H. Laaksovirta, J. C. van Swieten, L. Myllykangas, H. Kalimo, A. Paetau, Y. Abramzon, A. M. Remes, A. Kaganovich, S. W. Scholz, J. Duckworth, J. Ding, D. W. Harmer, D. G. Hernandez, J. O. Johnson, K. Mok, M. Ryten, D. Trabzuni, R. J. Guerreiro, R. W. Orrell, J. Neal, A. Murray, J. Pearson, I. E. Jansen, D. Sondervan, H. Seelaar, D. Blake, K. Young, N. Halliwell, J. B. Callister, G. Toulson, A. Richardson, A. Gerhard, J. Snowden, D. Mann, D. Neary, M. A. Nalls, T. Peuralinna, L. Jansson, V.-M. Isoviita, A.-L. Kaivorinne, M. Hölttä-Vuori, E. Ikonen, R. Sulkava, M. Benatar, J. Wuu, A. Chiò, G. Restagno, G. Borghero, M. Sabatelli, D. Heckerman, E. Rogaeva, L. Zinman, J. D. Rothstein, M. Sendtner, C. Drepper, E. E. Eichler, C. Alkan, Z. Abdullaev, S. D. Pack, A. Dutra, E. Pak, J. Hardy, A. Singleton, N. M. Williams, P. Heutink, S. Pickering-Brown, H. R. Morris, P. J. Tienari, B. J. Traynor, A hexanucleotide repeat expansion in *C9ORF72* is the cause of chromosome 9p21-linked ALS-FTD. *Neuron* **72**, 257–268 (2011).
63. M. DeJesus-Hernandez, I. R. Mackenzie, B. F. Boeve, A. L. Boxer, M. Baker, N. J. Rutherford, A. M. Nicholson, N. A. Finch, H. Flynn, J. Adamson, N. Kouri, A. Wojtas, P. Sengdy, G.-Y. R. Hsiung, A. Karydas, W. W. Seeley, K. A. Josephs, G. Coppola, D. H. Geschwind, Z. K. Wszolek, H. Feldman, D. S. Knopman, R. C. Petersen, B. L. Miller, D. W. Dickson, K. B. Boylan, N. R. Graff-Radford, R. Rademakers, Expanded GGGGCC hexanucleotide repeat in noncoding region of *C9ORF72* Causes chromosome 9p-linked FTD and ALS. *Neuron* **72**, 245–256 (2011).
64. R. Balendra, A. M. Isaacs, C9orf72-mediated ALS and FTD: Multiple pathways to disease. *Nat. Rev. Neurol.* **14**, 544–558 (2018).
65. C. Restif, C. Ibáñez-Ventoso, M. M. Vora, S. Guo, D. Metaxas, M. Driscoll, CeleST: Computer vision software for quantitative analysis of *C. elegans* swim behavior reveals novel features of locomotion. *PLOS Comput. Biol.* **10**, e1003702 (2014).
66. F. Frottin, M. Pérez-Berlanga, F. U. Hartl, M. S. Hipp, Multiple pathways of toxicity induced by *C9orf72* dipeptide repeat aggregates and G4C2 RNA in a cellular model. *eLife* **10**, e62718 (2021).
67. V. M. Advani, P. Ivanov, Stress granule subtypes: An emerging link to neurodegeneration. *Cell. Mol. Life Sci.* **77**, 4827–4845 (2020).
68. S. Jain, J. R. Wheeler, R. W. Walters, A. Agrawal, A. Barsic, R. Parker, ATPase-modulated stress granules contain a diverse proteome and substructure. *Cell* **164**, 487–498 (2016).
69. H. Ryu, G. Al-Ani, K. Deckert, D. Kirkpatrick, S. P. Gygi, M. Dasso, Y. Azuma, PIASy mediates SUMO-2/3 conjugation of poly(ADP-Ribose) polymerase 1 (PARP1) on mitotic chromosomes. *J. Biol. Chem.* **285**, 14415–14423 (2010).
70. F. Trulsson, V. Akimov, M. Robu, N. van Overbeek, D. A. P. Berrocal, R. G. Shah, J. Cox, G. M. Shah, B. Blagoev, A. C. O. Vertegaal, Deubiquitinating enzymes and the proteasome regulate preferential sets of ubiquitin substrates. *Nat. Commun.* **13**, 2736 (2022).
71. G. Grimaldi, G. Catara, L. Palazzo, A. Corteggio, C. Valente, D. Corda, PARPs and PAR as novel pharmacological targets for the treatment of stress granule-associated disorders. *Biochem. Pharmacol.* **167**, 64–75 (2019).

72. A. Messer, D. C. Butler, Optimizing intracellular antibodies (intrabodies/nanobodies) to treat neurodegenerative disorders. *Neurobiol. Dis.* **134**, 104619 (2020).
73. G. Liu, D. P. Xirodimas, NUB1 promotes cytoplasmic localization of p53 through cooperation of the NEDD8 and ubiquitin pathways. *Oncogene* **29**, 2252–2261 (2010).
74. O. Leidecker, D. P. Xirodimas, Isolation of NEDDylated proteins in human cells, in *Ubiquitin Family Modifiers and the Proteasome*, R. J. Dohmen, M. Scheffner, Eds. (Humana Press, 2012), vol. 832 of *Methods in Molecular Biology*, pp. 133–140.
75. K. T. Applegate, S. Besson, A. Matov, M. H. Bagonis, K. Jaqaman, G. Danuser, plusTipTracker: Quantitative image analysis software for the measurement of microtubule dynamics. *J. Struct. Biol.* **176**, 168–184 (2011).

Acknowledgments: We are grateful to the imaging facility MRI, member of the national infrastructure France-BioImaging infrastructure. We thank C. Hammell (Cold Spring Harbor Laboratory, USA) and P. Kratsios (University of Chicago Medical Center, USA) for providing the GFP/RFP-tagged *gtbp-1* and the *C9orf72 C. elegans* animals, respectively. We also thank M. Bonnet (Anne Debant's laboratory, CRBM) for providing mouse-derived hippocampal neurons and B. Vitre (Benedicte Delaval's laboratory, CRBM) for the EB1-mcherry–expressing retrovirus. S.C. and J.M. acknowledge AriSLA (Granulopathy and MLOpathy) for the generation and study of human fibroblast lines. Protocols and informed consent for the generation of the HDF20 and sALS 37/15 fibroblast lines were approved by the Institutional Ethics Committee [protocol no. 375/04 (7 January 2004) and protocol no. 299/14 (28 April 2015)]. We thank C. Cereda and O. Pansarasa for the generation of the human fibroblast lines. **Funding:** This work was funded by the following: Labex EpiGenMed, an « Investissements d'avenir » program, reference ANR-10-LABX-12-0; Postdoctoral fellowship to R.S. by Fondation Recherche Médicale (SPF202110013944); French National Research Agency (ANR-10-INBS-04, «Investments for the future»); Departments of excellence 2018–2022; E91I18001480001; and European commission, Horizon 2020 that supports the UbiCODE Research Training network. **Author contributions:** T.K. and R.S. performed most of the experiments. I.M. and A.B. identified and characterized the NEDDylation sites on PARP-1, including the generation of PARP-1 mutants. H.T. and J.P. assisted with the SG dynamics experiments, survival/clonogenic assays, and the generation of Nb9-expressing virus. R.S. and A.B. performed all experiments in *C. elegans*. J.M. and S.C. generated the ALS fibroblasts, and S.C. characterized SG dynamics in the fibroblast lines. D.P.X., with the help of all members, conceived and managed the project. D.P.X. wrote the manuscript with the assistance of S.C. **Competing interests:** A patent application for the used nanobody in this study has been submitted. The authors declare no other competing interests. **Data and materials availability:** All data needed to evaluate the conclusions in the paper are present in the paper and/or the Supplementary Materials. The raw files for the proteomics data S1 are available via ProteomeXchange with identifier PXD040466. The used nanobody in this study can be provided by D. Xirodimas pending scientific review and a completed material transfer agreement. Requests for the nanobody should be submitted to D. Xirodimas.

Submitted 28 April 2022
Accepted 27 February 2023
Published 31 March 2023
10.1126/sciadv.abq7585